

Review of Lattice Boltzmann Method Applied to Computational Aeroacoustics

Weidong SHAO⁽¹⁾, Jun LI^{(1),(2)*}

⁽¹⁾ *Institute of Turbomachinery, Xi'an Jiaotong University*
Xi'an 710049, China; e-mail: shilin1225@126.com

⁽²⁾ *Collaborative Innovation Centre of Advanced Aero-Engine*
Beijing 100191, China

*Corresponding Author e-mail: junli@mail.xjtu.edu.cn

(received July 22, 2018; accepted December 21, 2018)

This paper presents the research studies carried out on the application of lattice Boltzmann method (LBM) to computational aeroacoustics (CAA). The Navier-Stokes equation-based solver faces the difficulty of computational efficiency when it has to satisfy the high-order of accuracy and spectral resolution. LBM shows its capabilities in direct and indirect noise computations with superior space-time resolution. The combination of LBM with turbulence models also work very well for practical engineering machinery noise. The hybrid LBM decouples the discretization of physical space from the discretization of moment space, resulting in flexible mesh and adjustable time-marching. Moreover, new solving strategies and acoustic models are developed to further promote the application of LBM to CAA.

Keywords: lattice Boltzmann method; computational aeroacoustics; dispersion and dissipation; perfectly matched layers; discontinuous Galerkin method.

Nomenclature

A_f – numerical flux,
 Am – amplified factor,
 a – differential scheme coefficient,
 b – time discretization scheme coefficient,
 cf – numerical flux,
 c – dimensionless constant, time discretization scheme coefficient,
 E – total energy,
 \mathbf{e} – lattice velocity,
 \mathbf{F} – linear or non-linear function vector,
 f – wave velocity, velocity distribution function,
 \mathbf{f} – solution vector,
 \mathbf{g} – intermediate solution vector,
 h – total energy distribution function,
 i – imaginary unit, index number,
 j – index number,
 k – wavenumber,
 L – number of points left from a node,
 \mathbf{M} – matrix,
 n – algebraic precision,
 \mathbf{n} – normal vector pointing outwards,
 O – truncated term,

p – pressure,
 Q – auxiliary variable,
 R – number of points right from a node, gas constant,
 \mathbf{r} – particle position,
 s – number of stage,
 T – temperature,
 t – time,
 \mathbf{U} – conservative variable vector,
 \mathbf{u} – macro velocity,
 \mathbf{V} – primitive variable,
 \mathbf{W} – magnitude variation,
 x – component of coordinate system,
 α – differential scheme coefficient,
 β – coordinate transformation coefficient,
 Ω – non-overlapping domain, non-linear collision operator,
 ω – circular frequency,
 ψ – basis/test function,
 Δ – spacing, step,
 σ – damping coefficient,
 δ – Kronecker delta function,
 ρ – density,
 κ – thermal conductivity,
 τ – viscous stress, relaxation time,
 ξ – kinetic viscosity coefficient,
 γ – specific heat ratio.

Superscripts

- eq – equilibrium distribution function,
- n* – number of time steps,
- neq – non-equilibrium distribution function,
- T – transposition,
- ' – spatial derivative, perturbation,
- – volume averaged value, mean value,
- * – numerical flux,
- ^ – magnitude,
- ~ – filtered variable.

Subscripts

- a* – acoustic mode,
- B* – bulk,
- e* – direction of east, Euler flux, entropy mode,
- i* – the *i*-th variable,
- j* – the *j*-th variable,
- v* – viscous flux,
- w* – direction of west,
- α – lattice direction,
- 0 – uniform mean flow.

1. Introduction

1.1. Historical development of computational aeroacoustics

Due to limited capability of theoretical analysis, and huge cost and long periods of experimental investigation, numerical simulation has emerged as an efficient alternative tool for various industrial applications. With the rapid development of computer power, this trend is still upwards. When numerical simulation is combined with aeroacoustics, the discipline is named computational aeroacoustics (CAA).

CAA was formally brought forward on a workshop in 1992 (HARDIN, HUSSAINI, 1993). Before, the aeroacousticians are devoted to developing acoustic analogy, which was firstly proposed for jet noise (LIGHTHILL, 1952). The acoustic analogy provides an exact governing equation of noise generation away from the flow region. Then, Lighthill's equation was generalized in the presence of arbitrarily moving surfaces (FOWCS WILLIAMS, HAWKINGS, 1969). This is a major advance and the governing equation known as the FW-H equation shows excellent performance in the prediction of the noise of rotating blades such as propellers and helicopter rotors. To solve the FW-H equation, many sophisticated algorithms have been developed. The Farassat's formulas are widely used because of its exact derivation and simple format (FARASSAT, 1981).

Besides the acoustic analogy, the compressible variables can be split into fluctuations and their incompressible counterparts to evaluate noise propagation (HARDIN, POPE, 1994). This approach is similar to the linearized Euler equations (LEE) with noise source terms (BAILLY, JUVE, 2000). Methods based on Kirchhoff's integral as well as boundary element method combined with the acoustic Green's function repre-

sent other alternatives (FREUND *et al.*, 1996; MANOHA *et al.*, 1999).

The above-mentioned methods have certain features in common. Given the input of aerodynamic source in the near field, the output of sound in the far field can be immediately obtained. However, the drawback of these methods is obvious that:

- a) they are unable to calculate the noise source,
- b) the interaction between flow and sound has to be significantly weak or negligible.

To overcome the problem, direct computation of sound in both the near and far fields was proposed by the aeroacousticians. The key issue is how to capture accurately the near field aeroacoustics, which is discussed in the following Subsec. 1.2.

1.2. Recent development of computational aeroacoustics

From the late eighties, computational fluid dynamics (CFD) has been used to compute the acoustic source. However, the attempt was a failure because the underlying physics of aerodynamics and aeroacoustics are significantly different. The acoustic fluctuation is usually four orders of magnitude smaller than the mean flow (TAM, 1995; LELE, 1997). In addition, the acoustic propagation is inherently with low dispersion, low dissipation and long distance. CFD is more suited to calculate steady or low frequency unsteady flows while CAA is mostly used to compute unsteady flow noises with large spectral bandwidth. Therefore, the recent development of CAA is more on the following numerical aspects:

- a) high-order of accuracy, low-dispersion and low-dissipation (LDLD) spatial discretization schemes,
- b) LDLD and stable time-marching schemes,
- c) linear or non-linear non-reflecting boundary conditions (NRBC).

The nature description of aeroacoustics problems is the Navier-Stokes equations (NSE). With different ways of treating the spatial derivatives in NSE, the spatial discretization is mainly partitioned into three categories: finite difference method (FDM), finite volume method (FVM), and discontinuous Galerkin-finite element method (DG-FEM). To compare these spatial discretization methods in CAA, the first-order wave equation is taken for example,

$$\frac{\partial f}{\partial t} + cf' = 0, \tag{1}$$

where *c* is the dimensionless constant, the superscript prime – spatial derivative. With the uniform grid as shown in Fig. 1, the discretized forms of three methods are

$$\text{FDM: } f'_i + \sum_{j=L_1}^{R_1} \alpha_j f'_{i+j} = \frac{1}{\Delta x} \sum_{j=L_2}^{R_2} a_j f_{i+j} + O(\Delta x^n), \tag{2}$$

$$\text{FVM: } \frac{\partial \bar{f}}{\partial t} \Delta x + c[(Af)_e - (Af)_w] = 0, \quad (3)$$

$$\begin{aligned} \text{DG-FEM: } & \int_{\Omega_i} \left(\frac{\partial f}{\partial t} + cf' \right) \psi dx \\ & = \int_{\partial \Omega_i} \mathbf{n} \cdot [cf - (cf)^*] \psi dx, \quad (4) \end{aligned}$$

where L, R – number of points from the left and right stencils to node i ; α, a – differential scheme coefficients; the bar – the volume averaged value; Af, cf – the numerical fluxes; Δx – the grid spacing; Ω – the non-overlapping domain; n – the algebraic precision; \mathbf{n} – normal vector pointing outwards; ψ – basis/test functions.

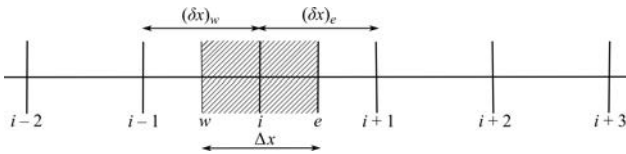


Fig. 1. Schematic of one-dimensional grid.

From Eq. (2), the Taylor/Fourier accuracy and numerical stability of FDM are determined by the stencil width and differential scheme coefficients. The flux construction based on Eq. (3) determines the algebraic/spectral accuracy of FVM. From Eq. (4), both the flux construction and test functions can determine the characteristics of DG-FEM. Obviously, these free parameters can be optimized to achieve better numerical performance. Table 1 (see Appendix A) gives the summaries of the main characteristics of three spatial discretization methods, respectively.

Although many excellent schemes have been proposed for spatial discretization, high-order formal accuracy, LDLD property for high wavenumber resolution, unconditional stability, and low computational cost have not yet been well satisfied. It still remains a challenge for the NSE-based spatial discretization. The resulting semi-discrete equation after spatial discretization is written

$$\frac{d\mathbf{f}}{dt} = \mathbf{F}(t, \mathbf{f}), \quad (5)$$

where \mathbf{f} – the solution vector for f ; \mathbf{F} – the linear or non-linear function vector constructed from the spatial discretization. It is common to use the Runge-Kutta (RK) methods for time-marching that

$$\mathbf{f}^{n+1} = \mathbf{f}^n + \Delta t \sum_{i=1}^s b_i \mathbf{g}_i, \quad (6)$$

$$\mathbf{g}_i = \mathbf{F} \left(\mathbf{f}^n + \Delta t \sum_{j=1}^s a_{ij} \mathbf{g}_j, t^n + c_i \Delta t \right), \quad i = 1, \dots, s, \quad (7)$$

where Δt – the time step; a_{ij}, b_i, c_i – the time discretization scheme coefficients. When $a_{ij} = 0$ for $i \leq j$,

the RK scheme is explicit. The implicit RK scheme requires non-zero a_{ij} for $i \leq j$. Among them, diagonally implicit RK scheme satisfies $a_{ij} = 0$ for $i < j$. Like the spatial discretization, the time discretization scheme coefficients can be optimized to achieve the LDLD property. The summaries of the main characteristics of the RK methods are given in Table 2 (see Appendix A).

High-resolution schemes do not guarantee high-accuracy results because of unphysical reflections from the artificial boundaries. NRBC plays a critical role in CAA and the widely used is divided into three kinds:

- a) Radiation boundary condition (RBC). It is based on the asymptotic expansion technique. RBC has been used for linear Euler equation, weakly non-linear equation and convective wave equation in exterior domains (TAM, WEBB, 1993; TAM, DONG, 1996; HAGSTROM *et al.*, 2003). RBC performs relatively well only when the acoustic source is far from the artificial boundary.
- b) Characteristics boundary condition (CBC). It is constructed from the eigenvalues of the Euler equation or NSE (THOMPSON, 1987; POINSOT, LELE, 1992). On the artificial boundary, local one-dimensional inviscid (LODI) relation is assumed and thus the acoustic wave propagates along the normal direction. Whether the waves are ingoing or outgoing is judged from the positive and negative eigenvalues. The magnitude of ingoing waves is set zero while the magnitude of outgoing waves is interpolated from the interior domain. Moreover, the multi-dimensional and viscous effects are supplemented (YOO, IM, 2007; LODATO *et al.*, 2008).
- c) Absorbing boundary condition (ABC). It adds buffer zones to the outside of the original computational domain. The flow field variables are damped to the preset values within the buffer zones to reduce the reflecting waves from the origin. Among ABC, perfectly matched layer (PML) attracted much attention because it ensures the consistent phase velocity and group velocity of physical waves within the buffer zones. In addition, the wavenumbers besides the interface are matched perfectly. PML was originally developed for magnetic wave radiation, and later applied to the Euler equation and NSE (HU, 2008; HU *et al.*, 2008).

1.3. Objective of this paper

So far, the spatial and temporal discretization methods as well as boundary conditions for CAA have concentrated on the solution of complete or simplified NSE. The numerical aspects are highly advanced, but some challenges still exists as discussed before. From the nineties, lattice Boltzmann method (LBM) has

emerged as an efficient tool for CFD. Much attention has been drawn because its formulation is significantly simple compared to the NSE-based methods such as Eqs (2)–(4):

$$f_\alpha(\mathbf{r} + \mathbf{e}_\alpha \Delta t, t + \Delta t) = f_\alpha(\mathbf{r}, t) + \Omega(f_\alpha), \quad (8)$$

where f_α (the bracket is neglected for simplicity) means the probability of finding a particle with the α -th lattice velocity \mathbf{e}_α at position \mathbf{r} at time t ; Ω – the non-linear collision operator. Obviously, the collision process is local while the streaming process is whole, which highly facilitates the implementation on parallel processing systems. Moreover, the boundary conditions including heuristic, kinetic and extrapolation schemes are easy. LBM has been widely applied to microfluidics, turbulence, multiphase flow, the suspension of particles and deformable capsules. A review of all publications pertaining to the LBM itself and its application to CFD would go beyond our space limitations. The interested readers are referred to the state-of-the-art reviews (CHEN, DOOLEN, 1998; YU *et al.*, 2003; HSU *et al.*, 2004; AIDUN, CLAUSEN, 2010).

LBM has also been applied to CAA because of its inherent high-resolution and efficiency, which will be discussed in the following. Though its application is still increasing, only the FDM-based LBM's application has been reviewed (TSUTAHARA, 2012). Consequently, this paper will provide detailed discussion and deep insight into the advantage and deficiency of LBM's applications as well as promising ways for CAA. Due to different underlying equations of aeroacoustics, the LBM-based methods are partitioned into two groups: direct acoustic computation with LBM (Sec. 2) and acoustic model based on LBM (Sec. 3). Finally, conclusions are drawn.

2. Direct acoustic computation with lattice Boltzmann method

2.1. Low-dispersion and low-dissipation capabilities of lattice Boltzmann method

Sound propagation simulations using lattice gas automata (LGA, the precursor of LBM) was firstly performed (SUDO, SPARROW, 1995). One-dimensional and two-dimensional lattices were developed to include dissipation. It also has an anisotropic dispersion, which increases with the increase of the propagating angle from the coordinate axes.

However, LGA has two drawbacks: the small number of discrete velocities leads to the statistical noise; the shear viscosity coefficient is limited to relatively high values. The development from LGA to LBM has gone through several stages. Although it was originally driven by its application to CFD, replacing LGA with LBM for CAA was accompanied. It underlines the

LDD capabilities of LBM to model the aeroacoustics problems, which is highly pursued for the NSE-based methods. Theoretical analysis and numerical tests have been used for wave propagation, streaming and scattering, spectral properties and resolution as well as direct and indirect models. Table 3 (see Appendix A) summarizes the properties of LBM and its modified schemes for CAA.

The earlier analysis and validation of LBM for CAA was mainly focused on the very low Mach number flow sound. Since many applications involve acoustic generation, propagation and scattering in compressible flows, it is necessary to examine the dispersion and dissipation relation of the compressible LBM. Here we take a plane wave propagating in the perfect gas for example. In order to obtain exact analytical solutions, all quantities $\mathbf{U} = (\rho, \rho u, \rho v, \rho w, \rho E)^T$ are firstly linearized as follows

$$\mathbf{U} = \mathbf{U}_0 + \mathbf{U}', \quad (9)$$

where the subscript 0 means the uniform flow, and the prime means the small amplitude perturbation. We neglect the second-order terms in the linearized equation to obtain

$$\frac{\partial \mathbf{U}'}{\partial t} + \frac{\partial [\mathbf{E}'_e - \mathbf{E}'_v]}{\partial x} + \frac{\partial [\mathbf{F}'_e - \mathbf{F}'_v]}{\partial y} + \frac{\partial [\mathbf{G}'_e - \mathbf{G}'_v]}{\partial z} = 0, \quad (10)$$

where the subscripts e and v indicate the Eulerian flux and viscous flux, respectively. The perturbation vector and six fluxes are given as follows

$$\mathbf{U}' = \begin{pmatrix} \rho' \\ \rho_0 u' \\ \rho_0 v' \\ \rho_0 w' \\ \rho_0 E' \end{pmatrix}, \quad \mathbf{E}'_e = \begin{pmatrix} \rho' u_0 + \rho_0 u' \\ \rho_0 u_0 u' + p' \\ \rho_0 u_0 v' \\ \rho_0 u_0 w' \\ (\rho_0 E' + p') u_0 + p_0 u' \end{pmatrix}, \quad (11)$$

$$\mathbf{F}'_e = \begin{pmatrix} \rho' v_0 + \rho_0 v' \\ \rho_0 v_0 u' \\ \rho_0 v_0 v' + p' \\ \rho_0 v_0 w' \\ (\rho_0 E' + p') v_0 + p_0 v' \end{pmatrix};$$

$$\mathbf{G}'_e = \begin{pmatrix} \rho' w_0 + \rho_0 w' \\ \rho_0 w_0 u' \\ \rho_0 w_0 v' \\ \rho_0 w_0 w' + p' \\ (\rho_0 E' + p') w_0 + p_0 w' \end{pmatrix}, \quad (12)$$

$$\mathbf{E}'_v = \begin{pmatrix} 0 \\ \tau'_{xx} \\ \tau'_{yx} \\ \tau'_{zx} \\ \tau'_{xx} u_0 + \tau'_{yx} v_0 + \tau'_{zx} w_0 + \kappa \frac{\partial T'}{\partial x} \end{pmatrix};$$

$$\mathbf{F}'_v = \begin{pmatrix} 0 \\ \tau'_{xy} \\ \tau'_{yy} \\ \tau'_{zy} \\ \tau'_{xy}u_0 + \tau'_{yy}v_0 + \tau'_{zy}w_0 + \kappa \frac{\partial T'}{\partial y} \end{pmatrix}, \quad (13)$$

$$\mathbf{G}'_v = \begin{pmatrix} 0 \\ \tau'_{xz} \\ \tau'_{yz} \\ \tau'_{zz} \\ \tau'_{xz}u_0 + \tau'_{yz}v_0 + \tau'_{zz}w_0 + \kappa \frac{\partial T'}{\partial z} \end{pmatrix},$$

where κ – the thermal conductivity. The linearized stress tensor is given

$$\tau'_{ij} = \rho_0 \xi \left(\frac{\partial u'_i}{\partial x_j} + \frac{\partial u'_j}{\partial x_i} - \frac{2}{3} \frac{\partial u'_k}{\partial x_k} \delta_{ij} \right) + \rho_0 \xi_B \frac{\partial u'_k}{\partial x_k} \delta_{ij}, \quad (14)$$

where ξ – the shear kinetic viscosity coefficient; ξ_B – the bulk kinetic viscosity coefficient. To complete Eq. (10), the perfect gas satisfying $p = \rho R_g T$ is used. Then by neglecting the second-order terms, the perturbed pressure and the perturbed total energy are obtained as follows

$$p' = \rho' R_g T_0 + \rho_0 R_g T', \quad (15)$$

$$E' = \frac{1}{\gamma - 1} R_g T' + u_0 u' + v_0 v' + w_0 w', \quad (16)$$

where γ – the specific heat ratio. Inserting Eqs (11)–(16) into Eq. (10), we can easily rewrite it as the following matrix form

$$\frac{\partial \mathbf{U}'}{\partial t} + \mathbf{M}_E \frac{\partial \mathbf{U}'}{\partial x} + \mathbf{M}_F \frac{\partial \mathbf{U}'}{\partial y} + \mathbf{M}_G \frac{\partial \mathbf{U}'}{\partial z} = 0, \quad (17)$$

where \mathbf{M}_E , \mathbf{M}_F , and \mathbf{M}_G are the resulting matrices (see Appendix B). The solutions for plane wave are usually written in the vector form

$$\mathbf{U}' = (\widehat{\rho}' \ \rho_0 \widehat{u}' \ \rho_0 \widehat{v}' \ \rho_0 \widehat{w}' \ \rho_0 \widehat{E}')^T \exp[i(\mathbf{k} \cdot \mathbf{x} - \omega t)], \quad (18)$$

where the accent indicates the complex values. Inserting Eq. (18) into Eq. (17) leads to the general eigenvalue problem

$$\omega \mathbf{U}' = (k_x \mathbf{M}_E + k_y \mathbf{M}_F + k_z \mathbf{M}_G) \mathbf{U}'. \quad (19)$$

Then the analytical solutions of Eq. (19) are readily obtained (see Appendix B).

Next, we examine the spectral properties of the discrete-velocity Boltzmann equation. For compressible flows, the DDF discrete-velocity Boltzmann equation is usually used. The gas equation of state and the

kinetic viscosity can be exactly recovered from the following equations with the Chapman-Enskog expansion

$$\frac{\partial f_\alpha}{\partial t} + \mathbf{e}_\alpha \cdot \nabla f_\alpha = \frac{1}{\tau_f} (f_\alpha^{\text{eq}} - f_\alpha),$$

$$\frac{\partial h_\alpha}{\partial t} + \mathbf{e}_\alpha \cdot \nabla h_\alpha = \frac{1}{\tau_h} (h_\alpha^{\text{eq}} - h_\alpha) - \frac{1}{\tau_{fh}} (\mathbf{e}_\alpha \cdot \mathbf{u}) (f_\alpha^{\text{eq}} - f_\alpha), \quad (20)$$

where h_α – the total energy distribution function; τ_f , τ_h , τ_{fh} – the relaxation times; the superscript eq indicates the equilibrium distribution function. The D3Q25 lattice model is used and the relaxation times satisfy: $1/\tau_{fh} = 1/\tau_h - 1/\tau_f$ (HE *et al.*, 2009). Similar to the decomposition of Eq. (9), the distribution function is divided into a uniform mean part and a fluctuating part that

$$f_\alpha = f_\alpha^{(0)} + f'_\alpha, \quad (21)$$

$$h_\alpha = h_\alpha^{(0)} + h'_\alpha.$$

Since the equilibrium distribution functions in Eq. (20) are still non-linear, it is difficult to conduct linear analysis. However, the Taylor expansion is adopted for the equilibrium distribution functions that

$$f_\alpha^{\text{eq}} = f_\alpha^{\text{eq},(0)} + \left. \frac{\partial f_\alpha^{\text{eq}}}{\partial f_\beta} \right|_{f_\beta=f_\beta^{(0)}} f'_\beta + \mathcal{O}((f'_\alpha)^2),$$

$$h_\alpha^{\text{eq}} = h_\alpha^{\text{eq},(0)} + \left. \frac{\partial h_\alpha^{\text{eq}}}{\partial h_\beta} \right|_{h_\beta=h_\beta^{(0)}} h'_\beta + \mathcal{O}((h'_\alpha)^2). \quad (22)$$

With the chain rule and moment conservation, the two partial derivatives in Eq. (22) can be immediately obtained as follows

$$\frac{\partial f_\alpha^{\text{eq}}}{\partial f_\beta} = \frac{\partial f_\alpha^{\text{eq}}}{\partial \rho} + \frac{\partial f_\alpha^{\text{eq}}}{\partial u} \frac{e_{\beta x} - u}{\rho}$$

$$+ \frac{\partial f_\alpha^{\text{eq}}}{\partial v} \frac{e_{\beta y} - v}{\rho} + \frac{\partial f_\alpha^{\text{eq}}}{\partial w} \frac{e_{\beta z} - w}{\rho}, \quad (23)$$

$$\frac{\partial h_\alpha^{\text{eq}}}{\partial h_\beta} = \frac{\partial h_\alpha^{\text{eq}}}{\partial E} \frac{1}{\rho}.$$

The fluctuating parts for both distribution functions are also written in the wave form like Eq. (18) that

$$(f'_\alpha \ h'_\alpha)^T = (\widehat{f}'_\alpha \ \widehat{h}'_\alpha)^T \exp[i(\mathbf{k} \cdot \mathbf{x} - \omega t)]. \quad (24)$$

Inserting Eq. (22) and Eq. (24) into Eq. (20) and neglecting the second-order terms result in the linear equation:

$$\omega \begin{pmatrix} \mathbf{f}' \\ \mathbf{h}' \end{pmatrix} = \begin{pmatrix} \mathbf{M}_f & \mathbf{0} \\ \mathbf{M}_{fh} & \mathbf{M}_h \end{pmatrix} \begin{pmatrix} \mathbf{f}' \\ \mathbf{h}' \end{pmatrix}, \quad (25)$$

where \mathbf{M}_f , \mathbf{M}_h , \mathbf{M}_{fh} – the components of eigenvalue matrix. These three matrices are

$$(\mathbf{M}_f)_{\alpha\beta} = \mathbf{k} \cdot \mathbf{e}_\alpha \delta_{\alpha\beta} + i \frac{1}{\tau_f} \left(\frac{\partial f_\alpha^{\text{eq}}}{\partial f_\beta} - \delta_{\alpha\beta} \right), \quad (26)$$

$$(\mathbf{M}_h)_{\alpha\beta} = \mathbf{k} \cdot \mathbf{e}_\alpha \delta_{\alpha\beta} + i \frac{1}{\tau_h} \left(\frac{\partial h_\alpha^{\text{eq}}}{\partial h_\beta} - \delta_{\alpha\beta} \right), \quad (27)$$

$$(\mathbf{M}_{fh})_{\alpha\beta} = -i \frac{1}{\tau_{fh}} (\mathbf{e}_\alpha \cdot \mathbf{u}_0) \left(\frac{\partial f_\alpha^{\text{eq}}}{\partial f_\beta} - \delta_{\alpha\beta} \right). \quad (28)$$

The explicit exact solutions of Eq. (19) and Eq. (25) is too lengthy to write down. But, the eigenvalues depend on these parameters, namely, the relaxation times, the wavenumber vectors and the mean flow parts. Since the lattice model D3Q25 is irregular, Eq. (20) has to be solved with FDM, FVM or DG-FEM instead of the standard collision and streaming steps. Then the more effective dispersion and dissipation relation of compressible LBM has to be analyzed by combining Eqs (2)–(4), which will be illustrated in the future paper.

2.2. Aeroacoustics engineering applications of lattice Boltzmann method

From Subsec. 2.1, it is clearly seen that the intrinsic LDD properties of LBM drives it an advanced tool for CAA. In this subsection, we review the practical engineering applications of LBM as well as its further improvement. Since the turbulence is usually involved in the sound source zone, it needs additional models for complete simulation. Compared to the NSE-based methods, LBM provides a convenient way to include the turbulence effect. By the Boussinesq assumption, the Reynolds/subgrid stress is expressed as the laminar viscosity stress, which treats the turbulence effect as certain viscosity. Consequently, the turbulent kinetic viscosity is easily incorporated into the collision model in Eq. (8).

The unsteady Reynolds-Averaged Navier-Stokes (URANS) model takes the phase average of the flow field, which can capture tones but neglect the broadband characteristics of the fluctuating information. Large eddy simulation (LES) model takes the space average of the flow field with the filter functions. The accuracy of LES depends on the filter width, which is more controllable than URANS. Even for the NSE-based CAA, LES shows better performance than URANS. From the following summary (Table 4, see Appendix A), the combination of LBM with LES model is more frequent. The engineering applications are more concentrated on the machinery noise, like the airframe noise, the rotor-stator tonal noise, and the jet noise.

LBM combined with turbulence models has been widely used for CAA. This trend is still upwards be-

cause of its faster computation compared to the NSE-based methods. From Eq. (8), LBM is essentially a Lagrangian meshless method. Moreover, all particles obey the same streaming rule, which transports one particle to its neighbors. The streaming process requires uniform square mesh at unit CFL number such that both $(\mathbf{r} + \mathbf{e}_\alpha \Delta t)$ and (\mathbf{r}) reside on the nodal points of the mesh, which is inherited from LGA. However, this brings some inherent disadvantages:

- a) the approximation to the curved boundary is low-order. The boundary shape for computation becomes a ladder, which may lose certain true physics,
- b) the time step is fixed and small. The streaming step requires that the particles pass to the neighbors with different lattice velocities during one time step. For high Reynolds number flow, the lattice length is significantly small, so is the time step. Therefore, the step number for time-marching has to be very large,
- c) the lattice length is identical over the whole computational domain. This could lead to huge degrees of freedom. Compared to the NSE-based methods, the excellent acceleration of LBM on parallel systems is counteracted to some extent. For the far acoustic field, the low frequency wave is dominated that using the same degrees of freedom as the near hydrodynamic field is a waste of computing resource.

In recent years, several efforts have been made to address the above problems because the discretization of physical space does not necessarily need to couple with the discretization of moment space (HE, LUO, 1997). Abandoning the collision and streaming steps, the researchers can solve the original discrete-velocity Boltzmann equation like Eq. (20) with various NSE-based methods, namely, FDM, FVM and FEM. Actually, these approaches are hybrid LBM and the characteristics of them is summarized in Table 5 (see Appendix A). We also abandon the standard streaming step in Eq. (8). The alternative way is to solve the following equivalent pure advection equation

$$\frac{\partial f_\alpha}{\partial t} + \mathbf{e}_\alpha \cdot \nabla f_\alpha = 0. \quad (29)$$

Here we take the combination of LBM with DG-FEM for example (SHAO, LI, 2018a). The key of the combination is the construction of the Lagrange-Euler frame. The collision step is maintained within the Lagrange coordinate system while the streaming step is solved within the Euler coordinate system. The one-dimensional form of Eq. (29) in one lattice direction is equivalent to Eq. (1). Thus, the DG-FEM form of Eq. (29) is analogy to Eq. (4). Obviously, the LDD properties of the standard streaming step have also been changed. The traditional schemes in Table 1 (see

Appendix A) as well as advanced interface fluxes can be used to increase the spectral resolution and LLDL properties. The brought advantage of the combination is the geometry adaptivity and flexible *hp* technology.

Actually, more than just releasing the streaming step, we also can release the collision step. With the Strang splitting method, the equation for velocity distribution function in Eq. (20) can be split into Eq. (29) and the following one

$$\frac{\partial f_\alpha}{\partial t} = \frac{1}{\tau_f} (f_\alpha^{\text{eq}} - f_\alpha). \quad (30)$$

Similarly, the above equation can be solved with FDM, FVM or DG-FEM. It is worth noting that the right hand side of Eq. (30) is significantly stiff because of the very small value of the relaxation time. For the semi-discrete form of Eq. (30), the time-marching schemes should be carefully chosen. The TVD, exponential or SSP properties in Table 2 (see Appendix A) are more suitable here for the temporal discretization.

The resulting equation for Eq. (29) or Eq. (30) after spatial discretization is the same as Eq. (5). Generally, the right hand side of Eq. (29) and Eq. (30) does not explicitly contain time. Further assuming that the semi-discrete operator of Eq. (5) is linear, substituting Eq. (6) and Eq. (7) into Eq. (5) yields

$$\mathbf{f}_\alpha^{n+1} = \mathbf{f}_\alpha^n + \Delta t \sum_{i=1}^s b_i \mathbf{g}_i, \quad (31)$$

$$\mathbf{g}_i = \frac{\partial \mathbf{f}_\alpha^n}{\partial t} + \Delta t \sum_{j=1}^s a_{ij} \frac{\partial \mathbf{g}_j}{\partial t}, \quad i = 1, \dots, s. \quad (32)$$

Considering the Fourier components in Eq. (24), the above two formulas can be rewritten as follows

$$\widehat{\mathbf{f}}_\alpha^{n+1} = \widehat{\mathbf{f}}_\alpha^n + \Delta t \sum_{i=1}^s b_i \widehat{\mathbf{g}}_i, \quad (33)$$

$$\widehat{\mathbf{g}}_i = -i\omega \widehat{\mathbf{f}}_\alpha^n - i\omega \Delta t \sum_{j=1}^s a_{ij} \widehat{\mathbf{g}}_j, \quad i = 1, \dots, s. \quad (34)$$

To evaluate the amplitude error and phase error of different RK schemes, an amplified factor is defined as

$$Am(\omega \Delta t) = \frac{\widehat{\mathbf{f}}_\alpha^{n+1}}{\widehat{\mathbf{f}}_\alpha^n}. \quad (35)$$

From Eq. (24), the exact solution of Am is $\exp[-i\omega \Delta t]$. The numerical solution of Am for the RK scheme can be obtained by solving Eq. (33) and Eq. (34).

Figure 2 shows the comparison of amplified factors between various RK schemes. The more the amplitude of the amplified factor approaches unit, the less dissipative the RK scheme is. In addition, the more the phase error of the amplified factor approaches zero, the less

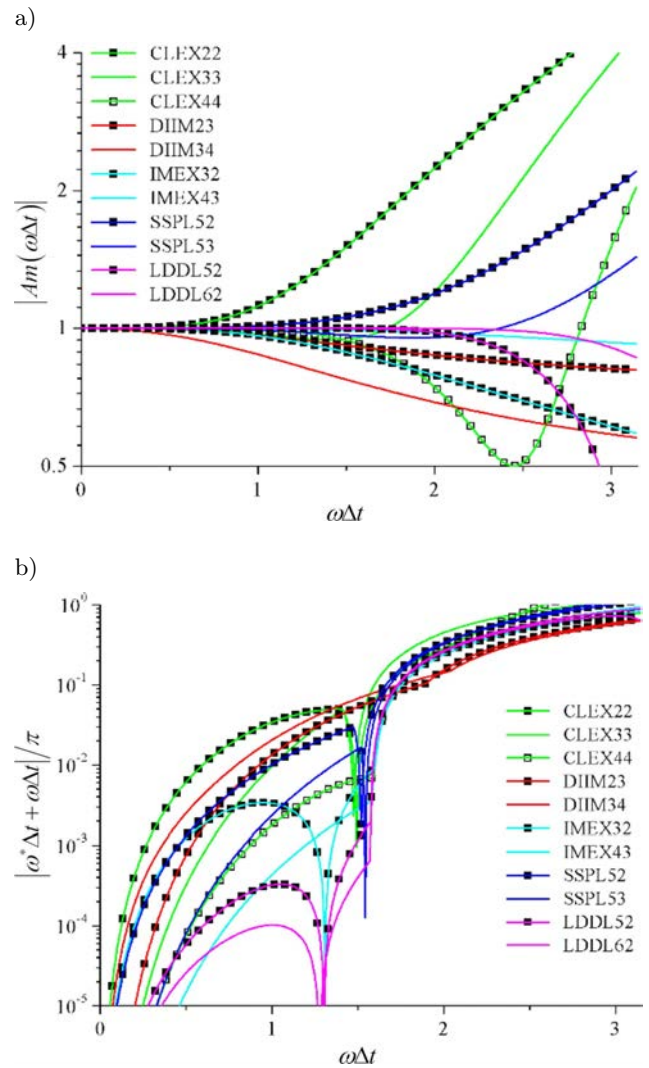


Fig. 2. Comparison of the amplified factors for different RK schemes: a) magnitude of Am , b) phase error of Am . In the legend: CLEX, DIIM, IMEX, SSPL, and LDDL means the classical explicit scheme, diagonally implicit scheme, implicit-explicit scheme, SSP and low storage scheme, and LDDL and low storage scheme, respectively. The first and second numbers indicate the number of stages and the precision accuracy. For example, CLEX33 represents the three-stages and third-order classical explicit RK scheme. The detailed RK coefficients are referred to the (SHAO, LI, 2018a).

dispersive the RK scheme is. It is obviously seen that LDDL52 and LDDL62 performs the best. The criteria to access the accuracy limit for the RK schemes is defined as follows

$$1 - |Am(\omega \Delta t)| \leq 5 \cdot 10^{-4} \quad (36)$$

$$\text{or } |\omega^* \Delta t + \omega \Delta t| / \pi \leq 5 \cdot 10^{-4}.$$

Then, the minimum periodicity for LDDL52 corresponds to $4.27\Delta t$ or $4.45\Delta t$ while the minimum periodicity for LDDL62 corresponds to $3.29\Delta t$ or $4.11\Delta t$.

In the future, the coupling methods may be more favorable. As the geometry and physical scales in the aeroacoustics engineering applications become more and more complicated, it is very difficult to gather all strong points like the LDLD property, high efficiency and so on by one single method. It is suggested that the standard LBM be adopted in the main flow region while the combination of LBM with the NSE-based methods be adopted in the boundary layer or complex flow/acoustics region. This strategy makes use of the quick calculation of LBM and the flexibility of the combination (of LBM with the NSE-based methods), as shown in Fig. 3. The data exchange between different methods as well as the optimization of the interface location should be paid close attention to.

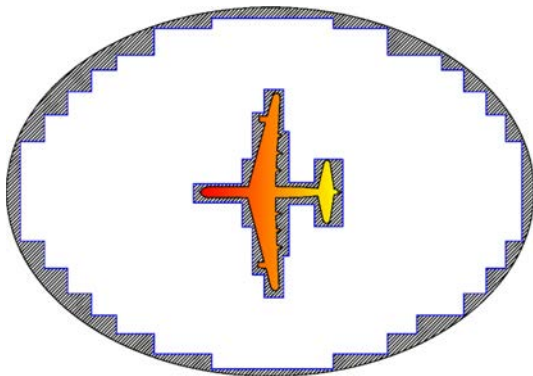


Fig. 3. Schematic of aircraft frame noise prediction using the coupling methods. The shadow region indicates where the combination of LBM with DG-FEM is used. The white area bounded with zigzags indicates where the standard LBM is used.

Besides the coupling algorithm, the turbulence models suitable for LBM need further study. So far, all turbulence models have been developed from NSE. For the kinetic method, the turbulence models may be developed from the Boltzmann equation itself, which would promote the ability of LBM.

3. Acoustic model based on lattice Boltzmann method

In Sec. 2, the macroscopic equations recovered from LBM is the Euler equation or incompressible/compressible NSE. Once the boundary conditions and the initial conditions are given, LBM can be self-starting and the unsteady hydrodynamic and aeroacoustics results would be finally obtained. Most results are well explained as long as the mesh and turbulence models are appropriate.

However, for the Euler equation or NSE with acoustic source terms, it is wrong to implement the standard LBM. The new acoustic model has to be constructed based on LBM. Even for aeroacoustics problems without given sources, the acoustic boundary condition,

i.e. NRBC, has to be constructed within the standard LBM framework. Thus, in this section we review the recent acoustic models based on LBM and give the potential methods to overcome the issue.

For monopole source, an easy and convenient way is replacing the velocity distribution function with its equilibrium distribution function, where the oscillating density is specified (XU *et al.*, 2012). However, the underlying flow is unphysically disturbed because the information contained in the non-equilibrium distribution functions is lost and overwritten at the node. In addition, it is impossible to extend it to the quadrupole source. The acoustic multiple source is implemented by adding an oscillating particle source term to the LBM equation, i.e. Eq. (8) (VIGGEN, 2013). When the source strength goes to zero, the source term naturally vanishes. But, the quadrupole strength is nonzero in the inviscid limit because of a fortuitous discretization error in the LBM. The analysis of LBM for linear acoustic waves is further done (DHURI *et al.*, 2017). It is found that the LBM's performance is comparable to the classical second-order finite difference schemes. The numerical dispersion is most inaccurate if the wave is propagating along the lattice direction. Recently, the acoustic multiple source method is developed to remove the dependency of the quadrupole source upon the fortuitous discretization error (ZHUO, SAGAUT, 2017). It is demonstrated that the regularized method with the regularized finite difference scheme can be used to simulate the acoustic problems very well.

The construction of acoustic multiple source is concentrated on the incompressible LBM. Obviously, the extension of acoustic multiple source method to the compressible LBM can be done in the future.

Whether the recovered equations from LBM are with or without multiple source terms, the LBM scheme has to be implemented with NRBC. NRBC allows the acoustic waves to go through the truncated boundaries without reflection and thus reduces the computational domain.

CBC firstly applied to LBM works well for one-dimensional flow but not for two-dimensional case of vortex shedding (IZQUIERDO, FUEYO, 2008). The problem was overcome by including the transverse terms with a convex combination in the CBC equations (HEUBES *et al.*, 2014). The extensions of conventional CBC to LBM lead to many spatial and temporal derivatives. This would introduce additional discretization error and decrease the numerical stability.

When the outgoing or incoming wave reaches the boundary, it is decomposed into the normal component and the tangential component, as illustrated in Fig. 4. The tangential component is maintained throughout. The normal component of the outgoing wave is maintained while the normal component of the incoming wave is diminished. Whether the normal component is incoming or not is judged from the

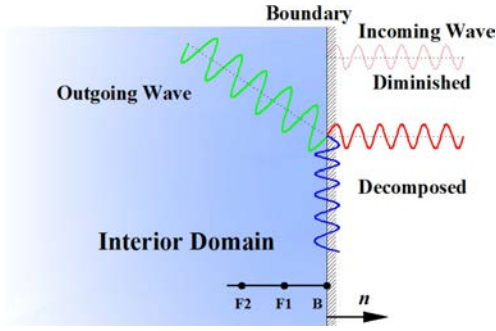


Fig. 4. Schematic of characteristic boundary condition.

characteristic theory. Since the characteristic theory is established for the hyperbolic system, the Euler equation has to be recovered on the boundary.

The Euler equation is written in the primitive variable vector as follows

$$\frac{\partial \mathbf{V}}{\partial t} + \mathbf{A} \frac{\partial \mathbf{V}}{\partial x} + \mathbf{B} \frac{\partial \mathbf{V}}{\partial y} + \mathbf{C} \frac{\partial \mathbf{V}}{\partial z} = 0, \quad (37)$$

where \mathbf{V} – the primitive variable, $\mathbf{V} = [\rho, u, v, w]^T$. The coefficient matrices are

$$\mathbf{A} = \begin{bmatrix} u & \rho & 0 & 0 \\ \rho^{-1}c_s^2 & u & 0 & 0 \\ 0 & 0 & u & 0 \\ 0 & 0 & 0 & u \end{bmatrix}, \quad \mathbf{B} = \begin{bmatrix} v & 0 & \rho & 0 \\ 0 & v & 0 & 0 \\ \rho^{-1}c_s^2 & 0 & v & 0 \\ 0 & 0 & 0 & v \end{bmatrix}, \quad (38)$$

$$\mathbf{C} = \begin{bmatrix} w & 0 & 0 & \rho \\ 0 & w & 0 & 0 \\ 0 & 0 & w & 0 \\ \rho^{-1}c_s^2 & 0 & 0 & w \end{bmatrix}.$$

Their diagonalization are

$$\mathbf{R}^{-1}\mathbf{A}\mathbf{R} = \mathbf{L}, \quad \mathbf{S}^{-1}\mathbf{B}\mathbf{S} = \mathbf{M}, \quad \mathbf{T}^{-1}\mathbf{C}\mathbf{T} = \mathbf{N}, \quad (39)$$

where \mathbf{L} , \mathbf{M} , \mathbf{N} – the eigenvalue matrices. These matrices can be easily obtained

$$\mathbf{L} = \text{diag}(u - c_s, u, u, u + c_s),$$

$$\mathbf{M} = \text{diag}(v - c_s, v, v, v + c_s), \quad (40)$$

$$\mathbf{N} = \text{diag}(w - c_s, w, w, w + c_s).$$

The positive eigenvalue indicates waves propagating in the positive $x/y/z$ direction while the negative eigenvalue indicates waves propagating in the negative $x/y/z$ direction. The direction of waves on the boundary can be immediately determined. From Eq. (39), the magnitude variation vectors are defined as

$$\mathbf{W}_x = \mathbf{L}\mathbf{R}^{-1} \frac{\partial \mathbf{V}}{\partial x}, \quad \mathbf{W}_y = \mathbf{M}\mathbf{S}^{-1} \frac{\partial \mathbf{V}}{\partial y}, \quad (41)$$

$$\mathbf{W}_z = \mathbf{N}\mathbf{T}^{-1} \frac{\partial \mathbf{V}}{\partial z}.$$

Inserting Eq. (41) into Eq. (37) yields

$$\frac{\partial \mathbf{V}}{\partial t} + \mathbf{R}\widetilde{\mathbf{W}}_x + \mathbf{S}\widetilde{\mathbf{W}}_y + \mathbf{T}\widetilde{\mathbf{W}}_z = 0, \quad (42)$$

where the wavy line means the filtered variables. The components of the filtered values are set to zero when the normal components are the incoming waves. Therefore, the controlling equation for CBC is Eq. (42). Moreover, LBM provides an easy way to implement CBC. The distribution functions are taken as their equilibrium distribution functions, where primitive variables are obtained from Eq. (42).

Besides the application of CBC to LBM, ABC has been applied to LBM. Adding a friction term to the discrete-velocity Boltzmann equation works well for simple test cases (KAM *et al.*, 2015). Then, the theoretical analysis of choosing the reference distribution functions was provided (XU, SAGAUT, 2013). Although an optimal absorbing strategy shows effective performance for vortical flows, the friction term could not guarantee the match of wave numbers at the interface between the interior domain and the sponge layer.

Based on the PML concept, a lattice Boltzmann model was developed for acoustic waves normally incident to the interface (TEKITECK *et al.*, 2009). The discrete-velocity Boltzmann equation can be recast in terms of perturbation components with the pseudo mean flow (CRAIG, HU, 2010). The pseudo mean flow satisfies:

- a) the steady Euler equation,
- b) it is aligned with one of the Cartesian coordinates.

The stability region can be determined with the Von Neumann analysis. Abandoning the above condition (b), an ABC model was introduced and a linear homogeneous hyperbolic system was obtained (NAYAFI-YAZDI, MONGEAU, 2012). A complete second-order temporal discretization of the resulting formulation with DG-FEM was further achieved (SHAO, LI, 2018b).

Figure 5 illustrates the schematic of PML, which damps the outgoing waves in the buffer zone and matches the wavenumbers at the interface. Within the PML, more than the acoustic perturbation is absorbed. The velocity distribution function in Eq. (20) is firstly decomposed into an equilibrium equation and a non-equilibrium equation:

$$\frac{\partial f_\alpha^{\text{eq}}}{\partial t} + \mathbf{e}_\alpha \cdot \nabla f_\alpha^{\text{eq}} = 0,$$

$$\frac{\partial f_\alpha^{\text{neq}}}{\partial t} + \mathbf{e}_\alpha \cdot \nabla f_\alpha^{\text{neq}} = -\frac{f_\alpha^{\text{neq}}}{\tau_f}, \quad (43)$$

where the superscript neq represents the non-equilibrium distribution function. Invoking the concept of time-independent pseudo mean flow, the equilibrium distribution function is partitioned into

$$f_\alpha^{\text{eq}} = \bar{f}_\alpha^{\text{eq}}(\bar{\rho}, \bar{\mathbf{u}}) + f_\alpha^{\prime \text{eq}}. \quad (44)$$

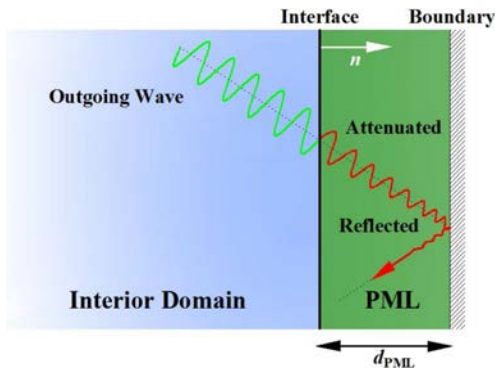


Fig. 5. Schematic of perfectly matched layer.

The only requirement for pseudo mean flow is

$$\mathbf{e}_\alpha \cdot \nabla \bar{f}'_\alpha = 0. \quad (45)$$

Using the Chapman-Enskog expansion again, the steady Euler equation is recovered. Since the pseudo mean flow is not unique, it could be chosen as accurate as possible to resemble the actual mean flow. Subtracting Eq. (45) from the Eq. (43) results in

$$\frac{\partial f'_\alpha}{\partial t} + \mathbf{e}_\alpha \cdot \nabla f'_\alpha = 0. \quad (46)$$

The above equation can be transformed in the frequency domain with the unsplit form as in the (SHAO, LI, 2018a)

$$-i\omega \hat{f}'_\alpha + \frac{e_{\alpha x}}{\omega + i\sigma_x} \frac{\partial \hat{f}'_\alpha}{\partial x} + \frac{e_{\alpha y}}{\omega + i\sigma_y} \frac{\partial \hat{f}'_\alpha}{\partial y} + \frac{e_{\alpha z}}{\omega + i\sigma_z} \frac{\partial \hat{f}'_\alpha}{\partial z} = 0, \quad (47)$$

where $\sigma_x, \sigma_y, \sigma_z$ – the positive damping coefficients.

Introducing the following two auxiliary variables,

$$\hat{P}_\alpha = \frac{i}{\omega} \hat{f}'_\alpha, \quad \hat{Q}_\alpha = \frac{i}{\omega} \hat{P}_\alpha, \quad (48)$$

Eq. (47) can be rewritten as

$$\begin{aligned} -i\omega \hat{f}'_\alpha + \mathbf{e}_\alpha \cdot \nabla \hat{f}'_\alpha &= -(\sigma_x + \sigma_y + \sigma_z) \hat{f}'_\alpha \\ &\quad - (\sigma_x \sigma_y + \sigma_x \sigma_z + \sigma_y \sigma_z) \hat{P}_\alpha \\ &\quad - e_{\alpha x} (\sigma_y + \sigma_z) \frac{\partial \hat{P}_\alpha}{\partial x} \\ &\quad - e_{\alpha y} (\sigma_x + \sigma_z) \frac{\partial \hat{P}_\alpha}{\partial y} \\ &\quad - e_{\alpha z} (\sigma_x + \sigma_y) \frac{\partial \hat{P}_\alpha}{\partial z} \\ &\quad - e_{\alpha x} \sigma_y \sigma_z \frac{\partial \hat{Q}_\alpha}{\partial x} - e_{\alpha y} \sigma_x \sigma_z \frac{\partial \hat{Q}_\alpha}{\partial y} \\ &\quad - e_{\alpha z} \sigma_x \sigma_y \frac{\partial \hat{Q}_\alpha}{\partial z} \\ &\quad - \sigma_x \sigma_y \sigma_z \hat{Q}_\alpha. \end{aligned} \quad (49)$$

With the inverse Fourier transform, Eq. (49) can be written into the time domain. Adding the non-equilibrium distribution function in Eq. (43) and Eq. (45) to the transformed equation yields

$$\begin{aligned} \frac{\partial f_\alpha}{\partial t} + \mathbf{e}_\alpha \cdot \nabla f_\alpha &= -(\sigma_x + \sigma_y + \sigma_z) f'_\alpha \\ &\quad - (\sigma_x \sigma_y + \sigma_x \sigma_z + \sigma_y \sigma_z) P_\alpha \\ &\quad + \frac{f_\alpha^{\text{eq}} - f_\alpha}{\tau_f} - e_{\alpha x} (\sigma_y + \sigma_z) \frac{\partial P_\alpha}{\partial x} \\ &\quad - e_{\alpha y} (\sigma_x + \sigma_z) \frac{\partial P_\alpha}{\partial y} \\ &\quad - e_{\alpha z} (\sigma_x + \sigma_y) \frac{\partial P_\alpha}{\partial z} \\ &\quad - e_{\alpha x} \sigma_y \sigma_z \frac{\partial Q_\alpha}{\partial x} - e_{\alpha y} \sigma_x \sigma_z \frac{\partial Q_\alpha}{\partial y} \\ &\quad - e_{\alpha z} \sigma_x \sigma_y \frac{\partial Q_\alpha}{\partial z} - \sigma_x \sigma_y \sigma_z Q_\alpha. \end{aligned} \quad (50)$$

The auxiliary variables Eq. (48) can also be written into the time domain

$$\frac{\partial P_\alpha}{\partial t} = f'_\alpha, \quad \frac{\partial Q_\alpha}{\partial t} = P_\alpha. \quad (51)$$

The ABC Eq. (50) is marched with the standard LBM or the NSE-based methods.

So far, respective studies for CBC and ABC applied to LBM have been done (HEUBES *et al.*, 2014; NAYAFI-YAZDI, MONGEAU, 2012; SHAO, LI, 2018a). The influences of free parameters in the controlling equations on the NRBC performance have been discussed in detail. CBC applied to LBM still suffers from the conventional corner problems. The reason for the unphysical reflections around the corner zones has not been clarified yet. Both the LODI assumption and the information loss of non-equilibrium distribution functions at the boundary may cause the corner problems. The comparison of CBC and ABC applied to the incompressible LBM has been done (STOLL, 2014). It was shown that PML combined with LBM had better NRBC performance than CBC combined with LBM.

However, PML applied to LBM also has some defects. Firstly, the turbulence intensity at the inlet or outlet can not be considered because the turbulent fluctuation is gradually damped to the given pseudo mean flow in the PML zone. Secondly, it increases the computational cost because of the auxiliary equations and the extended computational domain. Thirdly, the absorption only works for acoustic fluctuation when the mean flow is not aligned with one of the coordinates.

The first and second defects of PML applied to LBM are intrinsic while the third defect can be amended. As shown in Fig. 6, the mean flow is arbitrary and the absorption should work for all hydrodynamic and aeroacoustics fluctuations. The compu-

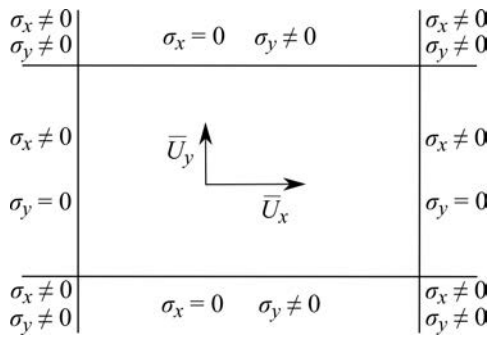


Fig. 6. PML constructed with arbitrary mean flow.

tational instability results from the inconsistent phase velocity and group velocity of hydrodynamic waves (HU, 2008). In order to remove the inconsistency, a new space-time transformation is introduced in the following.

Subtracting Eq. (45) from Eq. (43) results in

$$\frac{\partial f'_\alpha}{\partial t} + \mathbf{e}_\alpha \cdot \nabla f'_\alpha = -\frac{f'_\alpha}{\tau_f} - f'_\alpha. \quad (52)$$

The difference between Eq. (46) and Eq. (52) is the velocity distribution functions to be damped. Equation (46) focuses on the absorption of fluctuating equilibrium velocity distribution function while Eq. (52) concentrates on the absorption of fluctuating velocity distribution function. Consequently, PML constructed from Eq. (46) is deemed at the Euler level while PML constructed from Eq. (52) is deemed at the NSE level.

Taking the two-dimensional PML constructed in the x direction for example, the space-time transformation is

$$\begin{aligned} \tilde{x} &= x, \\ \tilde{t} &= t + \beta_x x, \quad \beta_x = \frac{\bar{U}_x}{c_s^2 - \bar{U}_x^2}, \\ \tilde{y} &= y - \bar{U}_y t, \end{aligned} \quad (53)$$

that gives

$$\begin{aligned} \frac{\partial}{\partial x} &= \frac{\partial}{\partial \tilde{x}} + \beta_x \frac{\partial}{\partial \tilde{t}}, \\ \frac{\partial}{\partial t} &= \frac{\partial}{\partial \tilde{t}} - \bar{U}_y \frac{\partial}{\partial \tilde{y}}, \\ \frac{\partial}{\partial y} &= \frac{\partial}{\partial \tilde{y}}. \end{aligned} \quad (54)$$

Substituting Eq. (54) into Eq. (52) yields

$$\begin{aligned} (1 + \beta_x e_{\alpha x}) \frac{\partial f'_\alpha}{\partial \tilde{t}} + e_{\alpha x} \frac{\partial f'_\alpha}{\partial \tilde{x}} \\ + (e_{\alpha y} - \bar{U}_y) \frac{\partial f'_\alpha}{\partial \tilde{y}} = -\frac{f'_\alpha}{\tau_f} - f'_\alpha. \end{aligned} \quad (55)$$

Similar to Eq. (47), Eq. (55) is written in the frequency domain with the unsplit form

$$\begin{aligned} -i\omega (1 + \beta_x e_{\alpha x}) \hat{f}'_\alpha + \frac{e_{\alpha x}}{1 + i\sigma_x \omega^{-1}} \frac{\partial \hat{f}'_\alpha}{\partial \tilde{x}} \\ + (e_{\alpha y} - \bar{U}_y) \frac{\partial \hat{f}'_\alpha}{\partial \tilde{y}} = -\frac{\hat{f}'_\alpha}{\tau_f} - \hat{f}'_\alpha. \end{aligned} \quad (56)$$

With the following auxiliary variables

$$\hat{P}_\alpha = \frac{i}{\omega} \hat{f}'_\alpha, \quad \hat{Q}_\alpha = \frac{i}{\omega} \hat{f}'_\alpha. \quad (57)$$

Using again the Fourier transform and Eqs (54), (56) and (57) can be written in the time domain

$$\begin{aligned} \frac{\partial f_\alpha}{\partial t} + \mathbf{e}_\alpha \cdot \nabla f_\alpha + (1 + \beta_x e_{\alpha x}) \sigma_x f'_\alpha \\ + (e_{\alpha y} - \bar{U}_y) \sigma_x \frac{\partial P_\alpha}{\partial \tilde{y}} + \frac{\sigma_x}{\tau_f} Q_\alpha = -\frac{f_\alpha}{\tau_f} - f_\alpha, \end{aligned} \quad (58)$$

$$\frac{\partial P_\alpha}{\partial t} + \bar{U}_y \frac{\partial P_\alpha}{\partial \tilde{y}} = f'_\alpha, \quad \frac{\partial Q_\alpha}{\partial t} + \bar{U}_y \frac{\partial Q_\alpha}{\partial \tilde{y}} = f'_\alpha. \quad (59)$$

Similarly, the PML in the y direction and corner can be easily constructed. Moreover, the numerical stability of PML applied to LBM needs further analysis and the involved free parameters can be reasonably chosen.

4. Conclusions and final remarks

The review of literature shows that the acoustic analogy does not allow us to calculate the noise source or the interaction between flow and noise. Aeroacousticians tried to compute directly flow noise with the common computational fluid dynamics methods, but failed because of the significant difference between aerodynamics and aeroacoustics. Sound is about four orders of magnitude lower than the mean pressure, with high bandwidth and long propagation distance. It requires that schemes used to solve the controlling equation be absolutely non-dispersive and non-dissipative.

The requirement is almost unreasonable considering the limited computational resources. Consequently, the spatial and temporal discretization has to be at least low-dispersive and low-dissipative (LDLD). The widely used methods (FDM, FVM and DG-FEM) in solving the Navier-Stokes equation (NSE) need optimization, mainly in terms of stencil width, differential scheme coefficient, flux construction and test functions. Many excellent schemes are discussed in Tables 1 and 2 (see Appendix A). The general principle is to decrease the magnitude error and phase error (of numerical schemes themselves) as much as possible. Meanwhile, the computational stability has to be maintained.

It is unfortunate that the computational efficiency is highly reduced when the NSE-based methods satisfy the LDLD property. The situation is remedied to a great extent by lattice Boltzmann method (LBM) because the LDLD property is inherent. For a given dispersion error, LBM is faster than the high-order

NSE-based schemes (MARIE *et al.*, 2009). A choice of 12–16 points per wavelength leads to reasonable numerical losses about 0.068 dB per wavelength (BRES *et al.*, 2009). The capabilities of direct and indirect models applied to computational aeroacoustics (CAA) are demonstrated based on rigorous tests with wave generation, propagation, streaming and scattering.

LBM also shows its potential in engineering machinery noise. In order to include the turbulence effect, several turbulence models are incorporated into LBM. The implementation is quite easy just by replacing the laminar viscosity with the equivalent viscosity. In addition, the large eddy simulation (LES) subgrid model is more frequently adopted because it is time accurate for the small scale turbulence structure. For many examples in Table 4 (see Appendix A), both the near hydrodynamic field and far acoustic field are accurately simulated. The numerical results from LBM match well with theoretical analysis, high-order NSE-based results or experiments.

LBM is essentially a Lagrangian meshless method in that all particles obey the same streaming rule inherited from lattice gas automata (LGA), which requires regular mesh at unit CFL number. However, this brings some limitations that the approximation to the curved boundary is low-order and the step number for time-marching has to be very large. Moreover, the lattice length is identical over the whole computational acoustic domain, leading to huge degrees of freedom. Actually, the discretization of physical space does not necessarily need to couple with the discretization of moment space (HE, LUO, 1997). Various NSE-based methods are adopted to solve the original discrete-velocity Boltzmann equation, which is the so-called hybrid LBM in Table 5 (see Appendix A).

Acoustic models based on LBM are divided into two kinds: model with acoustic multiple source and model combined with NRBC. The key of the first kind model is removing the dependency of the quadrupole source upon the fortuitous discretization error (ZHUO, SAGAUT, 2017). It is demonstrated that the regularized method with the regularized finite difference scheme can be used to simulate the acoustic problems very well. The second kind model is also partitioned into two kinds: CBC-LBM and ABC-LBM. CBC-LBM suffers from the conventional corner problems. Both the LODI assumption and the information loss of non-equilibrium distribution functions at the boundary may be the cause. For the case of low Mach number flow sound, ABC-LBM has better NRBC performance than CBC-LBM (STOLL, 2014). However, the turbulence intensity at the inlet or outlet can not be considered because the turbulent fluctuation is gradually damped to the given pseudo mean flow in the PML zone.

The authors try to present solving strategies and acoustic models to promote the application of LBM to CAA. The exact solution of plane wave propagation in compressible flows is obtained as Eq. (19). The dispersion and dissipation relation of compressible DDF LBM is examined. The standard streaming step can be released with the replace of DG-FEM (for the equivalent advection equation) to achieve the geometry adaptivity and flexible *hp* technology (SHAO, LI, 2018a). A coupling algorithm is proposed to make use of the quick calculation of LBM and the flexibility of combination (of LBM with the NSE-based methods). ABC with arbitrary mean flow based on perfectly matched layers at the Navier-Stokes level is developed.

Appendix A

Table 1. Summary of three spatial discretization methods' characteristics.

Method	Numerical scheme	Accuracy/stability	Description
FDM	Compact (LELE, 1992)	Spectral-like behavior.	It improves representation of a range of wavenumbers rather than accurate resolution of a single wave.
	Dispersison-Relation-Preserving (DRP) (TAM, WEBB, 1993)	Significant increase of the spectral resolution compared to the standard difference schemes.	It is guaranteed that the computed wave speeds, dispersion and isotropy are the same as those of the original partial derivative.
	Optimized Compact (KIM, LEE, 1996)	Multi-diagonal with high-order and high-resolution.	The phase errors are minimized in the wavenumber domain.
	Shock-fitting (ZHONG, 1998)	Less dissipative and high-order.	It adopts an upwind-bias grid stencil, and a high-order shock-fitting formulation.
	Optimized upwind DRP (ZHUANG, CHEN, 1998)	Much smaller dispersive and dissipative errors.	It improves the quality of numerical solutions without adding artificial selective damping terms.
	Compact spectral (LEE, SEO, 2002)	Wave resolution errors uniformly distributed in the wavenumber space.	An optimization in the wavenumber space does not guarantee the best performance.

Table 1. [Cont.]

Method	Numerical scheme	Accuracy/stability	Description
	Optimized prefactored compact (ASHCROFT, ZHANG, 2003)	Matching of their dispersion characteristics with those of central compact schemes.	It requires very small stencil support by splitting central implicit schemes into forward and backward biased operators.
	Non-centered FDM and selective filters (BERLAND <i>et al.</i> , 2007)	Highly accurate for waves with at least five points per wavelength.	It minimizes the dispersion and dissipation errors with the maximum order of accuracy.
FVM	Optimized compact-difference-based (GAITONDE, SHANG, 1997)	Combining the primitive function approach with five-point spatially sixth- and fourth-order methods.	It minimizes Fourier analysis-based dispersion and isotropy error functions for each wavenumber range of interest.
	DRP-based (POPESCU <i>et al.</i> , 2005)	Better solution of short waves while maintaining the pre-determined formal orders of accuracy.	It produces noticeably better solutions and handling the discontinuity or large gradients more satisfactorily.
	Symmetry preserving (KOK, 2009)	Fourth-order accurate and LDLD.	Kinetic energy, sound-velocity and internal energy are locally conserved by convection.
	Compact upwind (MURMAN, 2010)	Fourth- and fifth-order based on a variable reconstruction.	It demonstrates formal accuracy of the scheme, the resolution of a broad wavenumber spectrum.
	Compact interpolation (FOSSO P. <i>et al.</i> , 2010)	Formally sixth-order accurate in a preferred direction orthogonal to the interface and at most fourth-order accurate in the transversal.	It matches Taylor series expansions around the interface center and guarantees good spectral resolution and low computational costs.
	Energy preserving (CAPUANO <i>et al.</i> , 2015)	Up to a certain order of accuracy on both solution and energy conservation.	The properly constructed RK schemes are faster than the standard skew-symmetric schemes.
	Freestream preserving (XU <i>et al.</i> , 2016)	The order of metric polynomials lower than the order of accuracy of Gaussian quadrature.	The metrics should be evaluated by the conservative or symmetric conservative forms.
DG-FEM	Flux analysis (HU <i>et al.</i> , 1999)	Dissipation error is dominant with the upwind flux while it is zero with the center flux.	The orientation of element in a mesh introduces anisotropy in the phase speed and damping rate.
	Gauss and Gauss-Lobatto (GASSNER, KOPRIVA, 2011)	The Gauss scheme is more accurate than the Gauss-Lobatto scheme and needing fewer points per wavelength.	The Gauss scheme is more restricted in the explicit time step choice. The spectra depends on the boundary conditions applied.
	Non-uniform basis functions (LAHIVAARA, HUTTUNEN, 2011)	A relatively constant error level of the solution can be achieved for a given mesh.	The CFL number is small enough so that the error is dominated by the error in the spatial discretization.
	Posteriori subcell limiter (DUMBSER <i>et al.</i> , 2014)	It works well for arbitrary high-order of accuracy in space and time and that does not destroy the natural subcell resolution.	High-order discretization is achieved using a local space-time DG predictor to evolve the data locally in time within each cell.
	Kinetic energy preserving (GASSNER, 2014)	It improves the approximation quality for coarsely resolved non-linear acoustics.	The kinetic energy preservation is guaranteed by a suitable interface flux combined with the skew-symmetric formulation.
	Entropy-bounded (LV, IHME, 2015)	Stabilizing solution in the vicinity of discontinuities and retaining the optimal accuracy for smooth solutions.	It relies on a linear scaling operator so that it is unable to remove shock-triggered oscillations of smaller magnitude.
	Embedded (NGUYEN <i>et al.</i> , 2015)	It gives rise to a matrix system having the sparsity system of the statically condensed continuous scheme.	It does not provide the optimal convergence of the approximate gradient, resulting in lacking local conservativity.
	Positivity-preserving (ZHANG, 2017)	Preserving positivity of density and internal energy without losing local conservation or high-order accuracy.	It does not depend on how derivatives of solutions are approximated and does not produce excessive artificial viscosity.

Table 2. Summary of the RK methods' characteristics.

Numerical schemes	Description
LLDD low-storage (STANESCU, HABASHI, 1998)	It leaves useful information in the storage locations, by writing each successive stage on the same register without zeroing the previously held values.
Total variation diminishing (TVD) (GOTTLIEB, SHU, 1998)	Non-TVD but linearly stable RK time-marching can generate oscillations even for the TVD spatial discretization; second- and third-order optimal RK methods are with a CFL coefficient equal to one.
Strong-stability-preserving (SSP) (GOTTLIEB <i>et al.</i> , 2001)	Optimal explicit SSP linear RK methods are applied to the strong stability of coercive approximations; Explicit SSP multistep methods for non-linear problems; SSP property of implicit RK and multistep methods.
Optimal SSP (SPITERI, RUUTH, 2002)	By allowing the number of stages to differ from the order of the method, optimal SSP schemes are with better, more effective CFL coefficients than the standard SSP schemes.
Optimal LLDD (BOGEY, BAILLY, 2004)	It minimizes the dispersion and dissipation errors in the wavenumber space up to the high wavenumber corresponding to four points per wavelength.
Exponential (HOCKBRUCK, OSTERMANN, 2010)	It can be applied to problems characterized by a Jacobian that possesses eigenvalues with large negative real parts; highly oscillatory problems with purely imaginary eigenvalues of large modulus can be solved.
Non-uniform time-step (LIU <i>et al.</i> , 2010)	The value at the intermediate-stages on the elements neighboring such as interfaces are linearly coupled with minimal dissipation and dispersion errors to ensure correct communication of solutions on the interfaces of grids with different time step sizes.
Linearly implicit Rosenbrock (BASSI <i>et al.</i> , 2015)	It overcomes the severe time step restriction of explicit schemes and requires one Jacobian matrix evaluation per time step; it ensures the positivity of all thermodynamic variables at the discrete level.

Table 3. Summary of LBM's capabilities for CAA.

Type	Numerical schemes	Description
Wave generation, propagation, streaming, and scattering	For linear sound waves (BUICK <i>et al.</i> , 1998)	When the pressure variations are considered to be a small perturbation, LBM is in line with theoretical expressions for waves unbound or in a pipe.
	For non-linear sound waves (BUICK <i>et al.</i> , 2000)	It is demonstrated that LBM can deal with a range of problems in non-linear acoustics. However, simulations presented there are limited to progressive waves in an unbound media.
	Modelling acoustic streaming (HAYDOCK, YEOMANS, 2001; 2003; HAYDOCK, 2005)	Acoustic streaming and radiation force are due to a time-averaged momentum transfer from the acoustic waves. Using LBM to model the acoustic streaming produced by two plates of finite length, a complex object placed in the acoustic field, and the motion of particles is demonstrated.
	Thermal-acoustic scattering (KAM <i>et al.</i> , 2009)	The theoretical solution of acoustic scattering by a thermal disturbance with zero net heat gain/loss was derived. The validity and extent of gas-kinetic scheme was verified.
	Through porous media (HASERT <i>et al.</i> , 2011)	Acoustic wave generation and propagation in porous media is validated through a spinning vortex pair.
	Noise source identification (VERGNAULT <i>et al.</i> , 2013)	Based on a split of the lattice Boltzmann method into a mean and a perturbation component, the inherent instability of the time-reversed LBM is overcome.
	For acoustic flows (CHEN, REN, 2015)	Multi-relaxation-time (MRT) model coupled with far field boundary condition is used to study the non-linear characteristics of acoustic flows. Single and double layers of steady streaming can be well captured.
	For compressible flow sound (LI, ZHONG, 2016)	The potential energy double-distribution-function (DDF) LBM is validated through flows around circular cylinder and airfoil.
Resolution and spectral properties	Modified bulk viscosity (DELLAR, 2001)	By solving a linearized NSE, decaying sound waves using LBM with addition of viscosity are studied. The deviations introduced by the modified viscosity is better.
	Canonical acoustic waves (CROUSE <i>et al.</i> , 2006)	LBM can correctly reproduce basic acoustic phenomena. A basic grid solution requires at least 5.6 grid cells per wavelength.

Table 3. [Cont.].

Type	Numerical schemes	Description
	Dissipation and dispersion property (MARIE <i>et al.</i> , 2009)	By stability analysis, the comparison between isothermal and linearized NSE and LBM models was made. It proves the low dissipative capabilities of LBM compared to high-order NSE-based schemes. For a given dispersion error, LBM is faster than high-order schemes.
	Requirements for resolution (BRES <i>et al.</i> , 2009)	Deviation of LBM on the phase speed is almost identical to direct numerical simulation (DNS). A choice of 12–16 points per wavelength leads to reasonable numerical losses about 0.068 dB per wavelength.
	Validation of LBM (LAFITTE, PEROT, 2009)	The use of sponge zone reduces the magnitude of the acoustic reflections by 96%. The overall results both in terms of aerodynamics and acoustics can be correctly simulated.
	Optimal LDLD MRT (XU, SAGAUT, 2011)	The acoustic modes are decoupled from the shear modes with respect to zero-mean flows by optimizing free parameters. It annihilates the spurious waves and the isotropic error suffered from the original scheme and reduces the over-damping influence of the bulk viscosity on pressure waves.
	For adiabatic acoustics (LI, SHAN, 2011)	Providing the lattice and the distribution functions ensure adequate recovery of NSE, adiabatic sound waves can be accurately simulated at least at the low-frequency limit.
	Viscously damped waves (VIGGEN, 2011)	Through linearization analysis, acoustic waves which are viscously damped in space are studied. The phase velocities and amplitude ratios do not match theory well.
	For flow around obstacles (MACHROUKI <i>et al.</i> , 2012)	Spectral analysis shows an agreement between the numerical results and the experimental measurements in low and medium frequencies, but divergence at high frequencies.
	Moving boundary conditions (CHEN <i>et al.</i> , 2014)	Immersed boundary methods' smooth interpolation produces less disturbing spurious pressure waves than bounce-back methods'.
	Accuracy for sound diffraction (HAO <i>et al.</i> , 2016)	The maximum relative difference in acoustic pressure between numerical and analytical solutions is only about 20% among all.
Direct and indirect models	One-step direct simulation (LI <i>et al.</i> , 2006a; 2006b; KAM <i>et al.</i> , 2016)	The ideal gas equation of state and the temperature dependence of the first coefficient of viscosity were correctly recovered. It is demonstrated that the modified LBM possesses the same accuracy as DNS for CAA.
	For non-linear shock (DELLAR, 2008)	By introducing an entirely separate set of particle distribution functions, the macroscopic energy equation is correctly recovered for compressible flows including shock problems.
	Improved LBM model (FU <i>et al.</i> , 2008)	The state equation for diatomic gas is exactly recovered without invoking the small Mach number assumption. The viability and correctness of the modified equilibrium distribution functions is verified with comparison to DNS.
	FDM-based LBM (TSUTAHARA <i>et al.</i> , 2008)	It introduces a negative viscosity term to reduce viscosity and additional internal degree of freedom for diatomic gases. Speed of sound is exactly recovered. Reasonable results can be obtained even at the very low Mach number of 0.027.
	Multi-entropy-level (ZHANG <i>et al.</i> , 2011)	The use of isentropic equation makes the model simple and efficient. However, the dissipation and dispersion effects as well as NRBC are not considered.
	For isotropic turbulence sound (ZHOU, DONG, 2014)	The use of LBM-based DNS is efficient when it is combined with the Lighthill analogy. The assumption of compactness of source combined with the stochastic forcing model modifies acoustic properties and may lead to spurious noise.

Table 4. Summary of engineering applications of LBM.

Applications	Turbulence	Description
Trapezoidal wing (SATTI <i>et al.</i> , 2008)	Very LES (VLES)	Mean flow predictions of lift/drag, surface pressure distributions, noise sources and their relative strength provide excellent comparison with experiments.
Axisymmetric ducts (DA SILVA <i>et al.</i> , 2009)	None	The simulation results for the flow and acoustic fields of an unflanged pipe model issuing a subsonic jet into a stagnant fluid region agree well with theory and experiments.
HVAC blowers (FRANCK <i>et al.</i> , 2011)	VLES	Favorable comparison to measurements demonstrate the capability of LBM simulations to be used for optimizing blower and casing designs during the development stages.
Tandem cylinder (BRES <i>et al.</i> , 2012)	RNG k-e model with hybrid wall function	For the surface, flow field and radiated noise, simulation results are in good agreement with experimental data. The presence of the side plates reduces significantly the spanwise coherence and improves the comparison with experiments.
Partially covered cavities (DE JONG <i>et al.</i> , 2013)	Implicit LES (ILES)	Simulations with direct turbulent fluctuations introduced at the inlet exhibit the same resonance amplitude with experiments. However, large spanwise widths and included boundary layer direct turbulent fluctuations are not considered.
Bluff body (HAN <i>et al.</i> , 2013)	None	Utilizing blend radius can reduce the noise around bluff bodies.
Axial fan (LALLIER-DANIELS <i>et al.</i> , 2013)	RNG k-e model	The mean pressure on the pressure side of blade for the design flowrate agrees with experimental data. However, the grid is too coarse to overpredict 30% of the pressure rise.
High speed train (MESKINE <i>et al.</i> , 2013)	Unknown	LBM-based solver is used for the near field while the porous FW-H solver is used for the far field. It is indicated that simulations can be used as a design tool for far field noise levels.
Centrifugal fan (PEROT <i>et al.</i> , 2013)	VLES	The fan noise and heat exchanger effects are correctly modeled. Comparison of experiments and simulations show a very satisfying agreement. The obstruction reduces the tonal noise by 10–13 dB.
Fan blade (STADLER <i>et al.</i> , 2014)	LES	For most of 1/3-octave bands, the overall agreement between simulations and experiments is within ± 2 dB. The total reduction of sound power level is 1.3 dB(A).
Coaxial jet noise (CASALINO, LELE, 2014)	VLES	LBM is proven to capture both the flow field and the associated noise radiation. The mesh resolution and turbulence model on the shear layer instabilities need further analysis.
Circular orifice (JI, ZHAO, 2014)	LES	Results from theoretical analysis, simulations and experiments are in good agreement. The damping effect depends on the incident sound frequency, the orifice thickness and the bias flow Mach number.
Porous media (QI <i>et al.</i> , 2015)	None	It presents an interpolation-supplemented grid refinement method. However, a load balancing algorithm to account for the altered mesh topology is further needed.
Isolated axial fan (STRUM <i>et al.</i> , 2015)	VLES	The predicted spectrum agrees satisfactorily with the experimental data. The fan is very sensitive to the inflow conditions.
Full aircraft (FARES <i>et al.</i> , 2016)	VLES	The Reynolds number is 10.5 million. It is highlighted that finer geometrical details not captured at model scales have a non-negligible contribution to the far field noise signature.
Low-speed fan (MOREAU <i>et al.</i> , 2016)	VLES	Simulations are still too coarse and predict too wide wakes. It is suggested that the wall pressure statistics are hardly influenced by rotation in the trailing-edge region.
Outlet-guide-vane (SANJOSE <i>et al.</i> , 2017)	RNG k-e model	The detailed acoustic modal powers from simulations compare well with the analytical results for homogeneous and heterogeneous configurations.

Table 5. Summary of characteristics of hybrid LBM.

Type	Characteristics	Description
FDM-based	High order accuracy (REIDER, STERLING, 1995)	It allows coarser resolution for a given error or lower error for fixed resolution in comparison with the standard LBM. The fourth-order upwind scheme is used for spatial discretization and the fourth-order RK scheme for time discretization.
	Physical symmetry and lattice symmetry (CAO <i>et al.</i> , 1997)	Both symmetry is not necessary for recovering the correct macroscopic dynamics. The central difference scheme is applied for spatial discretization and the modified Euler method for time discretization.
	With curvilinear body-fitted coordinates (MEI, SHYY, 1998)	It can handle the boundary with desirable flexibility. The second-order central and upwind difference schemes are used for spatial discretization and the forward Euler method for time discretization.
	Numerical viscosity (SOFONEA, SEKERKA, 2003)	FDM-based LBM introduces a spurious numerical viscosity in the compressible regime. The standard LBM is recovered when the relaxation time is also calculated on the characteristics line.
	Implicit-explicit (WANG <i>et al.</i> , 2007)	The computational convergence rate can be significantly improved compared with the previous FDM-based and standard LBM. The TVD and weighted essentially non-oscillatory schemes are adopted for spatial discretization.
FVM-based	Structured mesh (NANNELLI, SUCCI, 1992)	The particle distribution function is stored on the cell center of control volume. The Poiseuille flow is applied for validation.
	Unstructured triangular mesh (XI <i>et al.</i> , 1999)	It can easily handle complex boundary geometries. It works well for Taylor vortex flow, shear flow between two parallel plates and cylinders as well as Poiseuille flow.
	Upwind scheme (STIEBLER <i>et al.</i> , 2006)	Discretizing the convective operator using upwind scheme demonstrates the improved stability and significant improvement in computational efficiency.
	TVD scheme (PATIL, LAKSHMISHA, 2009)	The discrete-velocity Boltzmann equation is discretized on a cell-centered, arbitrary shaped, triangular tessellation with the TVD scheme for terms representing advection. It is robust and accurate.
	Gas-kinetic BGK scheme (LI, LI, 2018)	The formal analytical solution of the lattice Boltzmann BGK equation is used to determine the flux on cell interfaces. The numerical dissipation is reduced.
FEM-based	Eulerian description (LEE, LIN, 2003)	The streaming step is carried out by solving the pure linear advection equations in an Eulerian framework. The speedup of convergence significantly improves with the implicit unstructured method.
	DG spectral element (SHI <i>et al.</i> , 2003)	It is used to solve the discrete-velocity Boltzmann equation with triangular elements because of their flexibility to deal with complex geometries.
	Least-squares element (LI <i>et al.</i> , 2005)	It enjoys fourth-order accuracy in space and second-order accuracy in time. The flexibility for complex geometries is demonstrated by a fluid flow in porous media.
	With an exponential time integrator (UGA <i>et al.</i> , 2013)	Using the spectral element DG to discretize the streaming step results in a system of ordinary differential equations, which is solved with an exponential time integrator. It can obtain high CFL number.
	Nodal DG scheme (ZADEHGOL <i>et al.</i> , 2014)	The streaming step is solved with nodal DG scheme and the time marching is carried out with low-storage fourth-order, five-stage RK method. It requires significantly lower number of grid points than the standard LBM.

Appendix B

Three matrices for the linearized NSE are

$$\mathbf{M_E} = \begin{pmatrix} u_0 & 1 & 0 & 0 & 0 \\ R_g T_0 & (2-\gamma)u_0 - \left(\frac{4}{3}\xi + \xi_B\right)\frac{\partial}{\partial x} & (1-\gamma)v_0 + \left(\frac{2}{3}\xi - \xi_B\right)\frac{\partial}{\partial y} & (1-\gamma)w_0 + \left(\frac{2}{3}\xi - \xi_B\right)\frac{\partial}{\partial z} & \gamma - 1 \\ 0 & -\xi\frac{\partial}{\partial y} & u_0 - \xi\frac{\partial}{\partial x} & 0 & 0 \\ 0 & -\xi\frac{\partial}{\partial z} & 0 & u_0 - \xi\frac{\partial}{\partial x} & 0 \\ R_g T_0 u_0 & a^* & b^* & c^* & d^* \end{pmatrix}, \quad (60)$$

where

$$\begin{aligned} a^* &= (1-\gamma)u_0^2 - \xi v_0 \frac{\partial}{\partial y} - \xi w_0 \frac{\partial}{\partial z} - \left[\frac{4}{3}\xi + \xi_B - \frac{(\gamma-1)\kappa}{\rho_0 R_g} \right] u_0 \frac{\partial}{\partial x} + R_g T_0, \\ b^* &= (1-\gamma)u_0 v_0 + \left(\frac{2}{3}\xi - \xi_B \right) u_0 \frac{\partial}{\partial y} - \left[\xi - \frac{(\gamma-1)\kappa}{\rho_0 R_g} \right] v_0 \frac{\partial}{\partial x}, \\ c^* &= (1-\gamma)u_0 w_0 + \left(\frac{2}{3}\xi - \xi_B \right) u_0 \frac{\partial}{\partial z} - \left[\xi - \frac{(\gamma-1)\kappa}{\rho_0 R_g} \right] w_0 \frac{\partial}{\partial x}, \\ d^* &= \gamma u_0 - \frac{(\gamma-1)\kappa}{\rho_0 R_g} \frac{\partial}{\partial x}; \end{aligned}$$

$$\mathbf{M_F} = \begin{pmatrix} v_0 & 0 & 1 & 0 & 0 \\ 0 & v_0 - \xi\frac{\partial}{\partial y} & -\xi\frac{\partial}{\partial x} & 0 & 0 \\ R_g T_0 & (1-\gamma)u_0 + \left(\frac{2}{3}\xi - \xi_B\right)\frac{\partial}{\partial x} & (2-\gamma)v_0 - \left(\frac{4}{3}\xi + \xi_B\right)\frac{\partial}{\partial y} & (1-\gamma)w_0 + \left(\frac{2}{3}\xi - \xi_B\right)\frac{\partial}{\partial z} & \gamma - 1 \\ 0 & 0 & -\xi\frac{\partial}{\partial z} & v_0 - \xi\frac{\partial}{\partial y} & 0 \\ R_g T_0 v_0 & e^* & f^* & g^* & h^* \end{pmatrix}, \quad (61)$$

where

$$\begin{aligned} e^* &= (1-\gamma)u_0 v_0 + \left(\frac{2}{3}\xi - \xi_B \right) v_0 \frac{\partial}{\partial x} - \left[\xi - \frac{(\gamma-1)\kappa}{\rho_0 R_g} \right] u_0 \frac{\partial}{\partial y}, \\ f^* &= (1-\gamma)v_0^2 - \xi u_0 \frac{\partial}{\partial x} - \xi w_0 \frac{\partial}{\partial z} - \left[\frac{4}{3}\xi + \xi_B - \frac{(\gamma-1)\kappa}{\rho_0 R_g} \right] v_0 \frac{\partial}{\partial y} + R_g T_0, \\ g^* &= (1-\gamma)v_0 w_0 + \left(\frac{2}{3}\xi - \xi_B \right) v_0 \frac{\partial}{\partial z} - \left[\xi - \frac{(\gamma-1)\kappa}{\rho_0 R_g} \right] w_0 \frac{\partial}{\partial y}, \\ h^* &= \gamma v_0 - \frac{(\gamma-1)\kappa}{\rho_0 R_g} \frac{\partial}{\partial y}; \end{aligned}$$

$$\mathbf{M}_{\mathbf{G}} = \begin{pmatrix} w_0 & 0 & 0 & 1 & 0 \\ 0 & w_0 - \xi \frac{\partial}{\partial z} & 0 & -\xi \frac{\partial}{\partial x} & 0 \\ 0 & 0 & w_0 - \xi \frac{\partial}{\partial z} & -\xi \frac{\partial}{\partial y} & 0 \\ R_g T_0 & (1 - \gamma) u_0 + \left(\frac{2}{3}\xi - \xi_B\right) \frac{\partial}{\partial x} & (1 - \gamma) v_0 + \left(\frac{2}{3}\xi - \xi_B\right) \frac{\partial}{\partial y} & (2 - \gamma) w_0 - \left(\frac{4}{3}\xi + \xi_B\right) \frac{\partial}{\partial z} & \gamma - 1 \\ R_g T_0 w_0 & i^* & j^* & k^* & l^* \end{pmatrix}, \quad (62)$$

where

$$\begin{aligned} i^* &= (1 - \gamma) u_0 w_0 + \left(\frac{2}{3}\xi - \xi_B\right) w_0 \frac{\partial}{\partial x} - \left[\xi - \frac{(\gamma - 1)\kappa}{\rho_0 R_g}\right] u_0 \frac{\partial}{\partial z}, \\ j^* &= (1 - \gamma) v_0 w_0 + \left(\frac{2}{3}\xi - \xi_B\right) w_0 \frac{\partial}{\partial y} - \left[\xi - \frac{(\gamma - 1)\kappa}{\rho_0 R_g}\right] v_0 \frac{\partial}{\partial z}, \\ k^* &= (1 - \gamma) w_0^2 - \xi u_0 \frac{\partial}{\partial x} - \xi v_0 \frac{\partial}{\partial y} - \left[\frac{4}{3}\xi + \xi_B - \frac{(\gamma - 1)\kappa}{\rho_0 R_g}\right] w_0 \frac{\partial}{\partial z} + R_g T_0, \\ l^* &= \gamma w_0 - \frac{(\gamma - 1)\kappa}{\rho_0 R_g} \frac{\partial}{\partial z}. \end{aligned}$$

The eigenvalues corresponding to Eq. (19) are

$$\begin{aligned} \omega_1 &= \omega_{a+}, \\ \omega_2 &= \omega_{a-}, \\ \omega_3 &= \mathbf{k} \cdot \mathbf{u}_0 - i\xi \mathbf{k}^2, \\ \omega_4 &= \mathbf{k} \cdot \mathbf{u}_0 - i\xi \mathbf{k}^2, \\ \omega_5 &= \omega_e, \end{aligned} \quad (63)$$

where ω_{a+} , ω_{a-} , and ω_e mean the acoustic modes and the entropy mode, respectively. ω_3 and ω_4 indicate the vorticity modes, which have simple expression. The dissipation of vorticity mode only comes from the shear kinetic viscosity. Since both viscosity and heat conductivity influence the propagation of the acoustic modes and entropy modes, the expressions for ω_1 , ω_2 , and ω_5 are complex. These eigenvalues are the three roots of the following equation

$$\begin{aligned} \omega'^3 - i(\eta + \varsigma) \mathbf{k}^2 \omega'^2 - (\eta \varsigma \mathbf{k}^2 + c_0^2) \omega' + i \frac{\varsigma}{\gamma} c_0^2 \mathbf{k}^4 &= 0, \\ \omega' = \mathbf{k} \cdot \mathbf{u}_0 - \omega, \quad \eta &= \frac{4}{3}\xi + \xi_B, \\ \varsigma &= (\gamma - 1) \frac{\kappa}{\rho_0 R_g}. \end{aligned} \quad (64)$$

Acknowledgements

This study has been funded by the National Natural Science Foundation (Grand No. 51776151) and Fundamental Research Funds for the Central Universities of China (Grand No. 2017YFB0601804). The authors

would like to thank the anonymous reviewers for their helpful and constructive comments. The first author wishes to thank his wife Yan CUI for her understanding while this manuscript was being prepared.

References

1. AIDUN C.K., CLAUSEN J.R. (2010), *Lattice-Boltzmann methods for complex flows*, Annual Review of Fluid Mechanics, **42**, 439–472.
2. ASHCROFT G., ZHANG X. (2003), *Optimized prefactored compact schemes*, Journal of Computational Physics, **190**, 2, 459–477.
3. BAILLY C., JUVE D. (2000), *Numerical solution of acoustic propagation problems using linearized Euler equations*, AIAA Journal, **38**, 1, 22–29.
4. BASSI F., BOTTI L., COLOMBO A., GHIDONI A., MASSA F. (2015), *Linearly implicit Rosenbrock-type Runge-Kutta schemes applied to the discontinuous Galerkin solution of compressible and incompressible unsteady flows*, Computers & Fluids, **118**, 305–320.
5. BERLAND J., BOGEY C., MARSDEN O., BAILLY C. (2007), *High-order, low dispersive and low dissipative explicit schemes for multiple-scale and boundary problems*, Journal of Computational Physics, **224**, 2, 637–662.
6. BOGEY C., BAILLY C. (2004), *A family of low dispersive and low dissipative explicit schemes for flow and noise computations*, Journal of Computational Physics, **194**, 1, 194–214.
7. BRES G.A., FREED D., WESSELS M. *et al.* (2012), *Flow and noise predictions for the tandem cylin-*

- der aeroacoustic benchmark, *Physics of Fluids*, **24**, 036101.
8. BRES G.A., PEROT F., FREED D. (2009), *Properties of the lattice-Boltzmann method for acoustic*, 15th AIAA/CEAS Aeroacoustics Conference and Exhibit, AIAA 09-3395, pp. 1–11, Miami, FL, USA.
 9. BUICK J.M., BUCKLEY C.L., GREATED C.A., GILBERT J. (2000), *Lattice Boltzmann BGK simulation of nonlinear sound waves: the development of a shock front*, *Journal of Physics A: General Physics*, **33**, 21, 3917–3928.
 10. BUICK J.M., GREATED C.A., CAMPBELL D.M. (1998), *Lattice BGK simulation of sound waves*, *Europhysics Letters*, **43**, 3, 235–240.
 11. CAO N.Z., CHEN S.Y., JIN S., MARTINEZ D. (1997), *Physical symmetry and lattice symmetry in the lattice Boltzmann method*, *Physical Review E*, **55**, 1, 21–24.
 12. CAPUANO F., COPPOLA G., BALARAC G., DE LUCA L. (2015), *Energy preserving turbulent simulations at a reduced computational cost*, *Journal of Computational Physics*, **298**, C, 480–494.
 13. CASALINO D., LELE S.K. (2014), *Lattice-Boltzmann simulation of coaxial jet noise generation*, *Proceedings of the Summer Program 2014*, 231–240.
 14. CHEN L., YU Y., LU J.H., HOU G.X. (2014), *A comparative study of lattice Boltzmann methods using bounce-back schemes and immersed boundary ones for flow acoustic problems*, *International Journal for Numerical Methods in Fluids*, **74**, 439–467.
 15. CHEN S.Y., DOOLEN G.D. (1998), *Lattice Boltzmann methods for fluid flows*, *Annual Review of Fluid Mechanics*, **30**, 329–364.
 16. CHEN X.P., REN H. (2015), *Acoustic flows in viscous fluid: A lattice Boltzmann study*, *International Journal for Numerical Methods in Fluids*, **79**, 4, 183–198.
 17. CRAIG E., HU F.Q. (2010), *On the perfectly matched layer for the Boltzmann-BGK equation and its application to computational aeroacoustics*, 16th AIAA/CEAS Aeroacoustics Conference and Exhibit, AIAA 10-3935, pp. 1–18, Stockholm, Sweden.
 18. CROUSE B., FREED D., BALASUBRAMANIAN G., SENTHOORAN S., LEW P.T., MONGEAU L. (2006), *Fundamental aeroacoustic capabilities of the lattice-Boltzmann method*, 12th AIAA/CEAS Aeroacoustics Conference and Exhibit, AIAA 06-2571, pp. 1–17, Cambridge, MA, USA.
 19. DA SILVA A.R., SCAVONE G.P., LEFEBVRE A. (2009), *Sound reflection at the open end of axisymmetric ducts issuing a subsonic mean flow: A numerical study*, *Journal of Sound and Vibration*, **327**, 507–528.
 20. DE JONG A.T., BIJL H., HAZIR A., WIEDEMANN J. (2013), *Aeroacoustic simulation of slender partially covered cavities using a lattice Boltzmann method*, *Journal of Sound and Vibration*, **332**, 1687–1703.
 21. DELLAR P.J. (2001), *Bulk and shear viscosities in lattice Boltzmann equations*, *Physical Review E*, **64**, 031203.
 22. DELLAR P.J. (2008), *Two routes from the Boltzmann equation to compressible flow of polyatomic gases*, *Progress in Computational Fluid Dynamics*, **8**, 1, 84–96.
 23. DHURI D.B., HANASOGE S.M., PERLEKAR P., ROBERTSSON J.O. (2017), *Numerical analysis of the lattice Boltzmann method for simulation of linear acoustic waves*, *Physical Review E*, **95**, 043306.
 24. DUMBSER M., ZANOTTI O., LOUBERE R., DIOT S. (2014), *A posteriori subcell limiting of the discontinuous Galerkin finite element method for hyperbolic conservation laws*, *Journal of Computational Physics*, **278**, 1, 47–75.
 25. FARASSAT F. (1981), *Linear acoustic formulas for calculation of rotating blade noise*, *AIAA Journal*, **19**, 9, 1122–1130.
 26. FARES E., DUDA B., KHORRAMI M.R. (2016), *Airframe noise prediction of a full aircraft in model and full scale using a lattice Boltzmann approach*, 22nd AIAA/CEAS Aeroacoustics Conference and Exhibit, AIAA 16-2707, pp. 1–21, Lyon, France.
 27. FFWOCS WILLIAMS J.E., HAWKINGS D.L. (1969), *Sound generation by turbulence and surfaces in arbitrary motion*, *Proceedings of the Royal Society of London Series A – Mathematical and Physical Sciences*, **264**, 1151, 321–342.
 28. FOSSO P.A., DENIAU H., SICOT F., SAGAUT P. (2010), *Curvilinear finite-volume schemes using high-order compact interpolation*, *Journal of Computational Physics*, **229**, 13, 5090–5122.
 29. FREUND J.B., LELE S.K., MOIN P. (1996), *Calculation of the radiated sound field using an open Kirchhoff surface*, *AIAA Journal*, **34**, 5, 909–916.
 30. FU S.C., SO R.M.C., LEUNG R.C.K. (2008), *Modelled Boltzmann equation and its application to direct aeroacoustics simulation*, *AIAA Journal*, **46**, 7, 1651–1662.
 31. GAITONDE D., SHANG J.S. (1997), *Optimized compact-difference-based finite-volume schemes for linear wave phenomena*, *Journal of Computational Physics*, **138**, 2, 617–643.
 32. GASSNER G.J. (2014), *A kinetic energy preserving nodal discontinuous Galerkin spectral element method*, *International Journal for Numerical Methods in Fluids*, **76**, 1, 28–50.
 33. GASSNER G., KOPRIVA D.A. (2011), *A comparison of the dispersion and dissipation errors of Gauss and Gauss-Lobatto discontinuous Galerkin spectral element methods*, *SIAM Journal on Scientific Computing*, **33**, 5, 2560–2579.
 34. GOTTLIEB S., SHU C.W. (1998), *Total variation diminishing Runge-Kutta schemes*, *Mathematics of Computation*, **67**, 221, 73–85.
 35. GOTTLIEB S., SHU C.W., TADMOR E. (2001), *Strong stability-preserving high-order time discretization methods*, *SIAM Review*, **43**, 1, 89–112.

36. HAGSTROM T., HARIHARAN S.I., THOMPSON D. (2003), *High-order radiation boundary conditions for the convective equations in exterior domains*, SIAM Journal on Scientific Computing, **25**, 3, 1088–1101.
37. HAN S.L., WANG G.S., YU L.S., WANG Y.Y. (2013), *Numerical simulation of two-dimensional bluff body aerodynamic noise using lattice Boltzmann method*, Advanced Materials Research, **610–613**, 2535–2538.
38. HAO J., KOTAPATI R.B., PÉROT F., MANN A. (2016), *Numerical studies of acoustic diffraction by rigid bodies*, 22nd AIAA/CEAS Aeroacoustics Conference and Exhibit, AIAA 16-2705, pp. 1–10, Lyon, France.
39. HARDIN J.C., HUSSAINI M.Y. (1993), *Computational aeroacoustics*, Springer-Verlag, New York.
40. HARDIN J.C., POPE D.S. (1994), *An acoustic/splitting technique for computational aeroacoustics*, Theoretical and Computational Fluid Dynamics, **6**, 5, 323–340.
41. HASERT M., BERNSDORF J., ROLLER S. (2011), *Towards aeroacoustic sound generation by flow through porous media*, Philosophical Transactions of the Royal Society A: Mathematical, Physical and Engineering Sciences, **369**, 1945, 2467–2475.
42. HAYDOCK D. (2005), *Lattice Boltzmann simulations of the time-averaged forces on a cylinder in a sound field*, Journal of Physics A: General Physics, **38**, 3265–3277.
43. HAYDOCK D., YEOMANS J.M. (2001), *Lattice Boltzmann simulations of acoustic streaming*, Journal of Physics A: General Physics, **34**, 5201–5213.
44. HAYDOCK D., YEOMANS J.M. (2003), *Lattice Boltzmann simulations of attenuation-driven acoustic streaming*, Journal of Physics A: General Physics, **36**, 5683–5694.
45. HE X., LUO L.S. (1997), *Theory of the lattice Boltzmann method: from the Boltzmann equation to the lattice Boltzmann equation*, Physical Review E, **53**, 6811–6817.
46. HE Y.L., WANG Y., LI Q. (2009), *Lattice Boltzmann method: Theory and applications* [in Chinese], Science Press, Beijing.
47. HEUBES D., BARTEL A., EHRHARDT M. (2014), *Characteristic boundary conditions in the lattice Boltzmann method for fluid and gas dynamics*, Journal of Computational and Applied Mathematics, **262**, 51–61.
48. HOCHBRUCK M., OSTERMANN A. (2010), *Exponential integrators*, Acta Numerica, **19**, 209–286.
49. HSU A.T., YANG T., LOPEZ I., ECER A. (2004), *A review of lattice Boltzmann models for compressible flows*, [in:] Chetverushkin B., Periaux J., Satofuka N., Ecer A. [Eds.], *Parallel Computational Fluid Dynamics 2003: Advanced Numerical Methods, Software and Applications*, Elsevier, pp. 19–28.
50. HU F.Q. (2008), *Development of PML absorbing boundary conditions for computational aeroacoustics: A progress review*, Computers & Fluids, **37**, 4, 336–348.
51. HU F.Q., HUSSAINI M.Y., RASETARINERA P. (1999), *An analysis of the discontinuous Galerkin method for wave propagation problems*, Journal of Computational Physics, **151**, 2, 921–946.
52. HU F.Q., LI X.D., LIN D.K. (2008), *Absorbing boundary conditions for nonlinear Euler and Navier-Stokes equations based on the perfectly matched layer technique*, Journal of Computational Physics, **227**, 9, 4398–4424.
53. IZQUIERDO S., FUEYO N. (2008), *Characteristic non-reflecting boundary conditions for open boundaries in lattice Boltzmann methods*, Physical Review E, **78**, 046707.
54. JI C.Z., ZHAO D. (2014), *Lattice Boltzmann investigation of acoustic damping mechanism and performance of an in-duct circular orifice*, Journal of the Acoustical Society of America, **135**, 6, 3243–3251.
55. KAM E.W.S., SO R.M.C., FU S.C. (2016), *One-step simulation of thermoacoustic waves in two-dimensional enclosures*, Computers & Fluids, **140**, 270–288.
56. KAM E.W.S., SO R.M.C., LEUNG R.C.K. (2009), *Acoustic scattering by a localized thermal disturbance*, AIAA Journal, **47**, 9, 2039–2052.
57. KAM E.W.S., SO R.M.C., LEUNG R.C.K. (2015), *Lattice Boltzmann method simulation of aeroacoustics and nonreflecting boundary conditions*, AIAA Journal, **45**, 7, 1703–1712.
58. KIM J.W., LEE D.J. (1996), *Optimized compact finite difference schemes with maximum resolution*, AIAA Journal, **34**, 5, 887–893.
59. KOK J.C. (2009), *A high-order low-dispersion symmetry-preserving finite-volume method for compressible flow on curvilinear grids*, Journal of Computational Physics, **228**, 18, 6811–6832.
60. LAFITE A., PÉROT F. (2009), *Investigation of the noise generated by cylinder flows using a direct lattice-Boltzmann approach*, 15th AIAA/CEAS Aeroacoustics Conference and Exhibit, AIAA 09-3268, pp. 1–12, Miami, FL, USA.
61. LAHIVAARA T., HUTTUNEN T. (2011), *A non-uniform basis order for the discontinuous Galerkin method of the acoustic and elastic wave equations*, Applied Numerical Mathematics, **61**, 4, 473–486.
62. LALLIER-DANIELS D., MOREAU S., SANJOSE M., PÉROT F. (2013), *Numerical analysis of axial fans for performance and noise evaluation using the lattice Boltzmann method*, CFD Canada 2013, Sherbrooke, Canada.
63. LEE C., SEO Y. (2002), *A new compact spectral scheme for turbulence simulation*, Journal of Computational Physics, **183**, 2, 438–469.
64. LEE T., LIN C.L. (2003), *An Eulerian description of the streaming process in the lattice Boltzmann equation*, Journal of Computational Physics, **185**, 445–471.

65. LELE S.K. (1992), *Compact finite difference scheme with spectral-like resolution*, Journal of Computational Physics, **103**, 1, 16–42.
66. LELE S.K. (1997), *Computational aeroacoustics – A review*, 35th Aerospace Sciences Meeting and Exhibit, AIAA 97-0018, pp. 1–15, Reno, NV, USA.
67. LI K., ZHONG C.W. (2016), *Aeroacoustic simulations using compressible lattice Boltzmann method*, Advances in Applied Mathematics and Mechanics, **8**, 5, 795–809.
68. LI W.D., LI W. (2018), *A gas-kinetic BGK scheme for the finite volume lattice Boltzmann method for nearly incompressible flow*, Computers & Fluids, **162**, 126–138.
69. LI X.M., LEUNG R.C.K., SO R.M.C. (2006a), *One-step aeroacoustics simulation using lattice Boltzmann method*, AIAA Journal, **44**, 1, 78–89.
70. LI Y.B., SHAN X.W. (2011), *Lattice Boltzmann method for adiabatic acoustics*, Philosophical Transactions of the Royal Society A: Mathematical, Physical and Engineering Sciences, **369**, 1944, 2371–2380.
71. LI Y.S., LEBOEUF E.J., BASU P.K. (2005), *Least-squares finite-element scheme for the lattice Boltzmann method on an unstructured mesh*, Physical Review E, **72**, 046711.
72. LI X.M., SO R.M.C., LEUNG R.C.K. (2006b), *Propagation speed, internal energy, and direct aeroacoustics simulation using lattice Boltzmann method*, AIAA Journal, **44**, 12, 2896–2903.
73. LIGHTHILL M.J. (1952), *On sound generated aerodynamically. I. General theory*, Proceedings of the Royal Society of London Series A – Mathematical and Physical Sciences, **211**, 1107, 564–587.
74. LIU L., LI X.D., HU F.Q. (2010), *Nonuniform time-step Runge-Kutta discontinuous Galerkin method for computational aeroacoustics*, Journal of Computational Physics, **229**, 19, 6874–6897.
75. LODATO G., DOMINGO P., VERVISCH L. (2008), *Three-dimensional boundary conditions for direct and large-eddy simulation of compressible viscous flows*, Journal of Computational Physics, **10**, 1, 5105–5143.
76. LV Y., IHME M. (2015), *Entropy-bounded discontinuous Galerkin scheme for Euler equations*, Journal of Computational Physics, **295**, 715–739.
77. MACHROUKI H., RICOT D., COSTE O. (2012), *Lattice Boltzmann aero-acoustics modelling of flow around obstacles*, Proceedings of the Acoustics 2012 Nantes Conference, 1297–1301, Nantes, France.
78. MANOHA E., ELIAS G., TROFF B., SAGAUT P. (1999), *Towards the use of boundary element method in computational aeroacoustics*, 5th AIAA/CEAS Aeroacoustics Conference and Exhibit, AIAA 99-1980, pp. 1161–1171, Bellevue, WA, USA.
79. MARIÉ S., RICOT D., SAGAUT P. (2009), *Comparison between lattice Boltzmann method and Navier-Stokes high order schemes for computational aeroacoustics*, Journal of Computational Physics, **228**, 4, 1056–1070.
80. MEI R.W., SHYY W. (1998), *On the finite difference-based lattice Boltzmann method in curvilinear coordinates*, Journal of Computational Physics, **143**, 426–448.
81. MESKINE M. et al. (2013), *Community noise prediction of digital high speed train using LBM*, 19th AIAA/CEAS Aeroacoustics Conference and Exhibit, AIAA 13-2015, pp. 1–17, Berlin, Germany.
82. MOREAU S., FOSS J., MORRIS S. (2016), *A numerical and experimental test-bed for low-speed fans*, Proceedings of the Institute of Mechanical Engineers Part A – Journal of Power and Energy, **230**, 5, 456–466.
83. MURMAN S.M. (2010), *Compact upwind schemes on adaptive octrees*, Journal of Computational Physics, **229**, 4, 1167–1180.
84. NANNELLI F., SUCCI S. (1992), *The lattice Boltzmann equation on irregular lattices*, Journal of Statistical Physics, **68**, 401–407.
85. NAYAFI-YAZDI A., MONGEAU L. (2012), *An absorbing boundary condition for the lattice Boltzmann method based on the perfectly matched layer*, Computers & Fluids, **68**, 203–218.
86. NGUYEN N.C., PERAIRE J., COCKBURN B. (2015), *A class of embedded discontinuous Galerkin methods for computational fluid dynamics*, Journal of Computational Physics, **302**, 674–692.
87. PATIL D.V., LAKSHMISHA K.N. (2009), *Finite volume TVD formulation of lattice Boltzmann simulation on unstructured mesh*, Journal of Computational Physics, **228**, 5262–5279.
88. PÉROT F. et al. (2011), *HVAC blower aeroacoustics predictions based on the lattice Boltzmann method*, Proceedings of the ASME-JSME-KSME 2011 Joint Fluids Engineering Conference, AJK 2011-23018, pp. 1–9, Hamamatsu, Shizuoka, Japan.
89. PÉROT F., KIM M.S., LE GOFF V., CARNIEL X., GOTH Y., CHASSAIGNON C. (2013), *Numerical optimization of the tonal noise of a backward centrifugal fan using a flow obstruction*, Noise Control Engineering Journal, **61**, 3, 307–319.
90. POINSOT T.J., LELE S.K. (1992), *Boundary conditions for direct simulations of compressible viscous flows*, Journal of Computational Physics, **101**, 104–129.
91. POPESCU M., SHYY W., GARBEY M. (2005), *Finite volume treatment of dispersion-relation-preserving and optimized prefactored compact schemes for wave propagation*, Journal of Computational Physics, **210**, 2, 705–729.
92. QI J.X., HASERT M., KLIMACH H., ROLLER S. (2015), *Aeroacoustic simulation of flow through porous media based on the lattice Boltzmann method*, [in:] Resch M., Bez W., Focht E. et al. [Eds.], *Sustained Simulation Performance*, pp. 195–204, Springer, Cham.
93. REIDER M.B., STERLING J.D. (1995), *Accuracy of discrete-velocity BGK models for the simulation of the incompressible Navier-Stokes equations*, Computers & Fluids, **24**, 4, 459–467.

94. SANJOSE M., MOREAU S., PESTANA M., ROGER M. (2017), *Effect of weak outlet-guide-vane heterogeneity on rotor-stator tonal noise*, AIAA Journal, **55**, 10, 3440–3457.
95. SATTI R., LI Y.B., SHOCK R., NOELTING S. (2008), *Aeroacoustics analysis of a high-lift trapezoidal wing using a lattice Boltzmann method*, 14th AIAA/CEAS Aeroacoustics Conference and Exhibit, AIAA 08-3048, pp. 1–16, Vancouver, British Columbia, Canada.
96. SHAO W.D., LI J. (2018a), *An absorbing boundary condition based on perfectly matched layer technique combined with discontinuous Galerkin Boltzmann method for low Mach number flow noise*, Journal of Theoretical and Computational Acoustics, **26**, 4, 1850011.
97. SHAO W.D., LI J. (2018b), *Three time integration methods for incompressible flows with discontinuous Galerkin Boltzmann method*, Computers & Mathematics with Applications, **75**, 11, 4091–4106.
98. SHI X., LIN J.Z., YU Z.S. (2003), *Discontinuous Galerkin spectral element lattice Boltzmann method on triangular element*, International Journal for Numerical Methods in Fluids, **42**, 1249–1261.
99. SOFONEA V., SEKERKA R.F. (2003), *Viscosity of finite difference lattice Boltzmann models*, Journal of Computational Physics, **184**, 422–434.
100. SPITERI R.J., RUUTH S.J. (2002), *A new class of optimal high-order strong-stability-preserving time discretization methods*, SIAM Journal on Numerical Analysis, **40**, 2, 469–491.
101. STADLER M., SCHMITZ M.B., LAUFER W., RAGG P. (2014), *Inverse aeroacoustic design of axial fans using genetic optimization and the lattice-Boltzmann method*, Journal of Turbomachinery, **136**, 041011.
102. STANESCU D., HABASHI W.G. (1998), *2N-storage low dissipation and dispersion Runge-Kutta schemes for computational acoustics*, Journal of Computational Physics, **143**, 2, 674–681.
103. STIEBLER M., TOLKE J., KRAFczyk M. (2006), *An upwind discretization scheme for the finite volume lattice Boltzmann method*, Computers & Fluids, **35**, 814–819.
104. STOLL S.J.B. (2014), *Lattice Boltzmann simulation of acoustic fields, with special attention to non-reflecting boundary conditions*, Master thesis, Norwegian University of Science and Technology.
105. STRUM M., SANJOSE M., MOREAU S., CAROLUS T. (2015), *Aeroacoustic simulation of an axial fan including the full test rig by using the lattice Boltzmann method*, Fan 2015, pp. 1–12, Lyon, France.
106. SUDO Y., SPARROW V.W. (1995), *Sound propagation simulations using lattice gas methods*, AIAA Journal, **33**, 9, 1582–1589.
107. TAM C.K.W. (1995), *Computational aeroacoustics: Issues and methods*, AIAA Journal, **33**, 10, 1788–1796.
108. TAM C.K.W., DONG Z. (1996), *Radiation and out-flow boundary conditions for direct computation of acoustic and flow disturbances in a nonuniform mean flow*, Journal of Computational Acoustics, **4**, 2, 175–201.
109. TAM C.K.W., WEBB J.C. (1993), *Dispersion-relation-preserving finite difference schemes for computational acoustics*, Journal of Computational Physics, **107**, 2, 262–281.
110. TEKITEK M.M., BOUZIDI M., DUBOIS F., LALLEMAND P. (2009), *Towards perfectly matching layers for lattice Boltzmann equation*, Computers & Mathematics with Applications, **58**, 5, 903–913.
111. THOMPSON K.W. (1987), *Time dependent boundary conditions for hyperbolic systems*, Journal of Computational Physics, **68**, 1, 1–24.
112. TSUTAHARA M. (2012), *The finite-difference lattice Boltzmann method and its application in computational aeroacoustics*, Fluid Dynamic Research, **44**, 045507.
113. TSUTAHARA M., KATAOKA T., SHIKATA K., TAKADA N. (2008), *New model and scheme for compressible fluids of the finite difference lattice Boltzmann method and direct simulations of aerodynamic sound*, Computers & Fluids, **37**, 1, 79–89.
114. UGA K.C., MIN M., LEE T., FISCHER P.F. (2013), *Spectral-element discontinuous Galerkin lattice Boltzmann simulation of flow past two cylinders in tandem with an exponential time integrator*, Computers & Mathematics with Applications, **65**, 239–251.
115. VERGNAULT E., MALASPINAS O., SAGAUT P. (2013), *Noise source identification with the lattice Boltzmann method*, The Journal of the Acoustical Society of America, **133**, 3, 1293–1305.
116. VIGGEN E.M. (2011), *Viscously damped acoustic waves with the lattice Boltzmann method*, Philosophical Transactions of the Royal Society A: Mathematical, Physical and Engineering Sciences, **369**, 1944, 2246–2254.
117. VIGGEN E.M. (2013), *Acoustic multiple source for the lattice Boltzmann method*, Physical Review E, **87**, 023306.
118. WANG Y., HE Y.L., ZHAO T.S., TANG G.H., TAO W.Q. (2007), *Implicit-explicit finite-difference lattice Boltzmann method for compressible flows*, International Journal of Modern Physics C, **18**, 12, 1961–1983.
119. PENG G.W., XI H.W., DUNCAN C. (1999), *Finite-volume scheme for the lattice Boltzmann method on unstructured meshes*, Physical Review E, **59**, 4, 4675–4682.
120. XU D., DENG X.G., CHEN Y.M., DONG Y.D., WANG G.X. (2016), *On the freestream preservation of finite volume method in curvilinear coordinates*, Computers & Fluids, **129**, 1, 20–32.

121. XU H., MALASPINAS O., SAGAUT P. (2012), *Sensitivity analysis and determination of free relaxation parameters for the weakly-compressible MRT-LBM schemes*, Journal of Computational Physics, **231**, 21, 7335–7367.
122. XU H., SAGAUT P. (2011), *Optimal low-dispersion low-dissipation LBM schemes for computational aeroacoustics*, Journal of Computational Physics, **230**, 13, 5353–5382.
123. XU H., SAGAUT P. (2013), *Analysis of the absorbing layers for the weakly-compressible lattice Boltzmann methods*, Journal of Computational Physics, **245**, 1, 14–42.
124. YOO C.S., IM H.G. (2007), *Characteristic boundary conditions for simulations of compressible reacting flows with multi-dimensional, viscous and reacting effects*, Combustion Theory and Modelling, **11**, 2, 259–286.
125. YU D.Z., MEI R.W., LUO L.S., SHYY W. (2003), *Viscous flow computations with the method of lattice Boltzmann equation*, Progress in Aerospace Sciences, **39**, 329–367.
126. ZADEHGOL A., ASHRAFIZADEH M., MUSAVI S.H. (2014), *A nodal discontinuous Galerkin lattice Boltzmann method for fluid flow problems*, Computers & Fluids, **105**, 58–65.
127. ZHANG J.Y., YAN G.W., YAN B., SHI X.B. (2011), *A lattice Boltzmann model for two-dimensional sound wave in the small perturbation compressible flows*, International Journal for Numerical Methods in Fluids, **67**, 214–231.
128. ZHANG X.X. (2017), *On positivity-preserving high order discontinuous Galerkin schemes for compressible Navier-Stokes equations*, Journal of Computational Physics, **328**, 301–343.
129. ZHONG X.L. (1998), *High-order finite-difference schemes for numerical simulation of hypersonic boundary-layer transition*, Journal of Computational Physics, **144**, 2, 662–709.
130. ZHOU Y.H., DONG Y.H. (2014), *An investigation of the lattice Boltzmann equation-based hybrid approach for simulation of sound generated by isotropic turbulence*, Computers & Fluids, **100**, 267–277.
131. ZHUANG M., CHEN R. (1998), *Optimized upwind dispersion-relation-preserving finite difference scheme for computational aeroacoustics*, AIAA Journal, **35**, 11, 2146–2148.
132. ZHUO C.S., SAGAUT P. (2017), *Acoustic multiple sources for the regularized lattice Boltzmann method: Comparison with multiple-relaxation-time models in the inviscid limit*, Physical Review E, **95**, 063301.